

Sulfur, sea salt, and radionuclide aerosols in GISS ModelE

Dorothy Koch,^{1,2} Gavin A. Schmidt,¹ and Christy V. Field^{1,2}

Received 26 October 2004; revised 3 May 2005; accepted 29 December 2005; published 29 March 2006.

[1] We simulate a suite of aerosols in the new GISS ModelE GCM: present-day sulfur species and the natural species sea salt, radionuclides ^7Be (stratospheric source), and ^{210}Pb (derived from ^{222}Rn from soils). The natural species are used to test the model and to help diagnose the anthropogenic sulfur species. Model improvements over previous versions include increased vertical resolution, addition of a stratiform dissolved species budget (DSB), better tracer coupling to the boundary layer, and an improved relative humidity-dependent radiative scheme. The DSB reduces the loads of most soluble species since it increases stratiform precipitation scavenging. We compare the model with extensive surface and aircraft concentration measurements in the troposphere and stratosphere. We compare three different formulations of the ^{222}Rn emissions and find that a scheme with reduced radon flux at high latitudes of the Northern Hemisphere for all seasons gives the best ^{210}Pb results. Although the ^{222}Rn emissions appear to be approximately the right order of magnitude, model ^{210}Pb is too large. Conversely, our ^7Be source is too small (since concentrations in the upper troposphere and stratosphere are deficient), while the ^7Be surface concentrations are as observed. These radionuclide results suggest that model scavenging (by moist convection) is deficient. Our new model uses increased natural sulfur emissions; however, the DSB causes sulfate to be generally less than observed and indicates a need for additional sulfur oxidation mechanisms. Model radiative forcing for sulfate and sea salt are -0.54 and -1.1 W m^{-2} , respectively. The anthropogenic sulfate forcing is -0.25 W m^{-2} , less than the -0.68 W m^{-2} in our previous model mainly owing to an 18% decrease in industrial emissions.

Citation: Koch, D., G. A. Schmidt, and C. V. Field (2006), Sulfur, sea salt, and radionuclide aerosols in GISS ModelE, *J. Geophys. Res.*, 111, D06206, doi:10.1029/2004JD005550.

1. Introduction

[2] There is an ongoing requirement to upgrade and improve aerosol model simulations in order to effectively model aerosol impacts on climate. Aerosols affect climate by reflecting and/or absorbing radiation and by influencing cloud reflectivity and lifetime. Thus the addition of human-produced sulfate, which is reflective, brightens the lower atmosphere and cools the surface. In addition it is believed to increase cloud droplet number and decrease cloud droplet size, causing an increase in cloudiness and cloud brightness, again cooling Earth's surface. The magnitude of these effects remain poorly constrained.

[3] A second purpose for modeling aerosol species is to improve our understanding of atmospheric processes and their representation in models. Historically, the study of radionuclides has been used for this purpose. Cosmogenic radionuclides, produced by spallation of cosmic rays on nitrogen and oxygen atoms in the lower stratosphere and

upper troposphere, have been used to constrain the flux from these regions to Earth's surface. Beryllium-7, with its 53-day half-life, is often used in atmospheric studies. It attaches to aerosol particles, so that it is a tracer of particle flux from the upper troposphere and stratosphere. Another useful atmospheric aerosol tracer series are the decay products of ^{222}Rn (radon), a gas emitted from continental soils. Radon decays ($t_{1/2} = 3.8$ days) to aerosol-associated species, including ^{210}Pb ($t_{1/2} = 22$ y). Thus ^{210}Pb makes a useful tracer of surface and continental sources. Both ^7Be and ^{210}Pb decay by gamma emission, a process easy to measure, so observations are relatively abundant. Radon has also been used in studies of convective transport [e.g., Jacob and Prather, 1990; Allen *et al.*, 1996]. A previous transport model based on the GISS-GCM was used to simulate ^{210}Pb [Balkanski *et al.*, 1993; hereinafter referred to as B93]. B93 demonstrated that convective transport processes needed to be coupled to convective precipitation scavenging processes in order to efficiently scavenge ^{210}Pb from the lowest model layer. In a subsequent study [Koch *et al.*, 1996; hereinafter referred to as K96] we added ^7Be to the ^{210}Pb model of B93 and found that the model did not scavenge enough ^7Be in tropical regions because, we argued, it lacked convective entrainment.

[4] Here we describe our latest generation of aerosol simulation in the new GISS GCM version known as

¹NASA Goddard Institute for Space Studies, New York, New York, USA.

²Also at Center for Climate Systems Research, Columbia University, New York, New York, USA.

ModelE. This model includes improvements in the GCM and tracer treatment therein (described in the work of *Schmidt et al.* [2006]) as well as implementation of new aerosol emissions and parameterizations. Mechanical improvements include increased modularity and flexibility. We revisit the radionuclide tracers, together with the sulfur species and sea salt. Simulating these together helps us discern the various source and sink processes that affect the aerosol concentrations. Thus, for example, it has been previously suggested that the radon- ^{210}Pb pair might act as analogs to the SO_2 -sulfate pair. Radon and SO_2 are both relatively short-lived gases derived primarily from continental source regions that transform to aerosols. We also look at the natural wind-derived oceanic species dimethylsulfide (DMS) and sea salt together. All aerosol species considered here are believed to be fully soluble and 100% uptake of aerosols within the cloudy portion of a grid box is assumed. As in our previous studies we model aerosol mass and we assume our aerosols are externally mixed. With the exception of sea salt, we do not simulate aerosol size.

[5] Our model vertical resolution is increased (from 9 to 20 layers). Our treatment of species dissolved in stratiform clouds is more sophisticated, so that we now save the dissolved fraction for the duration of the cloud lifetime. Our previous model versions [*Koch et al.*, 1999; K96] like many other global aerosol models, returned dissolved species to the cloud-free portion of the grid box after each cloud time step (e.g., each model 30 minutes for this simulation). A dissolved species budget (DSB) was used in the work of *Koch et al.* [2003] and we found this resulted in a decreased sulfate burden since the scheme allows more precipitation scavenging. We showed that the DSB made the cloud-sulfate correlation more negative, consistent with observed anticorrelation. We also use a new radiative scheme that includes the relative humidity-dependence of radiative parameters for sulfate and sea salt [*Schmidt et al.*, 2006].

[6] Numerous global sulfur model studies exist. Many of these are summarized in the model intercomparison papers of *Barrie et al.* [2001], *Lohmann et al.* [2001], and *Roelofs et al.* [2001]. More recent models include *Rotstayn and Lohmann* [2002], *Chin et al.* [2000a, 2000b], *Barth et al.* [2000], *Rasch et al.* [2000b], *Takemura et al.* [2000] and *Berglen et al.* [2004]. We will compare our model with a representative sample of these as well as with our own previous sulfur model.

[7] Our previous sulfur model [*Koch et al.*, 1999; hereinafter referred to as K99] was generally successful at producing observed sulfate surface concentrations especially near continental source regions. On average, it was about 10% above observed surface concentrations in North America and about 30% below observed surface concentrations in Europe. Remote, oceanic locations were deficient by about 50%, which was attributed to deficient production from DMS. Our new model differs in many respects from K99. We use new emissions, including a DMS windspeed parameterization that generates more DMS over oceans. We use a larger steady volcanic SO_2 source. In addition, we use a new SO_2 fossil fuel emission inventory, appropriate for the year 2000.

[8] Our radionuclide simulations also differ from that of K96. In addition to the GCM model improvements, we

work with new sources. In K96 we used the ^7Be source of *Lal and Peters* [1967] that was based on observations from a peak solar activity year (the cosmogenic source strength is anticorrelated with solar activity). Here we use the calculated source of *Masarik and Beer* [1999] for an average solar year. We plan to use this source for climate studies in which we will vary the solar strength and so will need to calculate the cosmogenic source corresponding to variable solar conditions. Thus the present study documents this present-day (^7Be) radionuclide climatology. We work with 3 radon emissions. The first is that of B93 (also used in K96). In addition we use the reduced (NH) high-latitude radon emissions recommended by *Conen and Robertson* [2002]. Second, we use the more detailed, seasonally and globally varying emission of *Schery and Wasiolek* [1998].

[9] We will compare this new model with our previous radionuclide model (K96) and with other previous radionuclide studies. These include the ^{210}Pb studies of *Lee and Feichter* [1995], *Feichter et al.* [1991], and model intercomparison studies of *Rasch et al.* [2000a] and *Barrie et al.* [2001]. Beryllium-7 has been modelled previously by *Land and Feichter* [2003] and *Brost et al.* [1991]. The ^{210}Pb and ^7Be pair were modeled by *Liu et al.* [2001] and *Rehfeld and Heimann* [1995].

[10] Sea salt is an important component of the global aerosol burden. Often, especially near polluted regions, other aerosol species are observed to be mixed with sea salt. For example, sea salt may act as a sink for SO_2 in polluted plumes from continents, thereby depleting the sulfate load over the oceans [e.g., *Zhuang et al.*, 1999]. However, few modeling studies have focused on sea salt and few measurements exist to constrain the models. Here we use a wind-based parameterization [*Monahan et al.*, 1986] similar to other model studies [e.g., *Chin et al.*, 2002; *Gong et al.*, 1997]. While other models have included many sea salt size bins (4–10), we attempt to obtain an adequate simulation with only 2 bins. The larger bin is roughly supermicron (dry), settles out rapidly, and is not important radiatively. It is, however, needed for comparison with observations. The smaller (submicron) bin is radiatively important, settles less rapidly, but still has a relatively short lifetime due to efficient precipitation scavenging in the marine boundary layer. Our primary purpose is to capture the radiative effects of sea salt. Modeling chemical interaction with other aerosols or gases would require more detailed surface area information.

2. Model Description

[11] The ModelE version of the GISS GCM is substantially different than the previous version (GISS Model II') used to simulate the sulfur species (K99). We briefly outline differences of most relevance to our tracers and refer to *Schmidt et al.* [2006] for further details. We use 20 vertical layers and $4^\circ \times 5^\circ$ horizontal resolution (latitude \times longitude). The model top is 0.1 mb and the resolution in the boundary layer is approximately doubled that in our previous 9-layer model: the bottom 4 levels are centered on 974, 949, 909 and 847 mb, compared with 959 and 894 mb in the lowest 2 layers of the 9-layer model. As in previous versions, the quadratic upstream scheme is used for transport of tracers, along with humidity and heat.

[12] Simulated species include (gaseous) dimethylsulfide (DMS), (particulate) methanesulfonic acid (MSA), (gaseous) sulfur dioxide (SO_2), (particulate) sulfate, (gaseous) hydrogen peroxide (H_2O_2), sea salt, the (particulate) radionuclides ^7Be and ^{210}Pb and the (gaseous) radionuclide ^{222}Rn .

[13] Near the surface, the tracers are handled using the same turbulent exchange coefficients as the model humidity. Turbulent dry deposition and interactive surface sources define the surface boundary conditions. The dry deposition scheme is based on the previously used resistance-in-series scheme (K99) derived from the Harvard GISS-CTM [e.g., *Chin et al.*, 1996]. The scheme is now more coupled to the model boundary layer processes and uses the previous scheme only to calculate the deposition velocity between the surface (10 m) layer and the ground.

[14] We include aerosol gravitational settling. Sea-salt aerosols are hydrated, according to the function given by *Gerber* [1985]. A term is included to allow settling of fine aerosols in the stratosphere where the air mean-free-path exceeds the particle radius [*Koch and Rind*, 1998].

[15] Some cloud-related features are similar to the previous version of the GISS aerosol model (e.g., K99). The model contains 2 cloud types, stratiform and convective. Following the corresponding cloud processes, the species are transported, dissolved, evaporated, and “scavenged” (with cloud water autoconversion and by raindrop impaction beneath clouds). In the model, convective cloud lifetime does not extend beyond the cloud time step; however, the stratiform cloud lifetime can be longer, extending until the cloud evaporates. A flaw in earlier aerosol simulations (e.g., K99 and K96) was the failure to retain dissolved species along with stratiform cloud water between (cloud) time steps. Instead the dissolved species were returned to the cloud-free portion of the grid box at the end of the cloud time step and then (re-)dissolved into the same cloud at the beginning of the next time step. In the new dissolved species budget (DSB) scheme, the dissolved species are retained in a stratiform budget, allowing release from the cloud to the clear air only as the cloud evaporates. (Further) dissolution of soluble species is permitted only in proportion to cloud growth, rather than allowing species in distant portions of the grid box to continue to dissolve into the cloud. This is appropriate because clouds are confined to the air mass in which they form and should not be permitted access to species in the cloud-free portion of a model grid box. (Note that our reported atmospheric burden or concentration includes only the cloud-free portions.) The DSB makes our tracer simulation more faithful to the cloud scheme and is therefore more physically realistic. As we will demonstrate below, sulfate is especially impacted by the DSB treatment since it is formed via aqueous phase oxidation in the cloud, as well as scavenged by cloud water precipitation. We included such a budget for sulfate in the work of *Koch et al.* [2003] and noted that the DSB reduced the sulfate burden. This is because the sulfate dissolved and/or produced in-cloud has less opportunity to escape the cloud; the dissolved sulfate is more likely to get removed with precipitation. While *Koch et al.* [2003] did include a dissolved-sulfate budget, ModelE includes such a budget for all soluble and partially soluble species (including SO_2 and H_2O_2). Another change from our previous model

versions is that we now assume 5% solubility in ice clouds (previous versions assumed zero solubility).

[16] We use an improved aerosol radiation scheme that includes the uptake of water by hygroscopic species such as sulfate and sea salt [*Schmidt et al.*, 2005]. The water uptake alters the particle size and scattering efficiency. The radiative effects of the consequent size and scattering changes vary with wavelength. The degree of hydration is saved as a function of space, allowing us to capture some of the hysteresis associated with deliquescence. However, the hydration state is not advected along with the aerosols. Unlike our previous sulfate studies [K99; *Koch*, 2001] that capped the impact of relative humidity (on optical thickness and therefore radiative forcing) at 0.85 the new scheme permits impact up to relative humidities of 0.999.

[17] The treatment of sulfur gas and aqueous phase chemistry is almost identical to that in K99. As before, we treat H_2O_2 semiprognostically and use input fields needed to generate and remove H_2O_2 (its photolysis rate, HO_2 , and OH). These fields (also NO_3 needed for DMS oxidation) are now taken from the ModelE gas chemistry [*Bell et al.*, 2005]. These are based on monthly mean three-dimensional (3-D) fields. One minor change in the chemistry is an increase in the H_2O_2 Henry’s law coefficient from 730 to 986.9 in order to be consistent with the value assumed in the ModelE chemistry.

3. Emissions

[18] As in the work of K99, we base our DMS emissions on the sea-water DMS concentrations of *Kettle et al.* [1999]. However, we now make use of the sea-to-air transfer function of *Nightingale et al.* [2000], together with model-generated surface (10 m) windspeeds. Since the dependence of the flux on the square of the windspeed is increased, our DMS emission (see Table 1) is approximately double that in the work of K99. We use this larger emission in order to increase the model sulfate production in remote regions closer to the observed levels.

[19] Our SO_2 industrial and volcanic emissions are those used by the AEROCOM model-observation intercomparison. The industrial SO_2 emission is from International Institute for Applied Systems Analysis (IIASA) (Frank Dentener, manuscript in preparation, 2004; Markus Amann, personal communication, 2004). It is a country-based SO_2 emission, gridded according to the EDGAR3.2 1995 (Emission Database for Global Atmospheric Research) distribution. It is similar to the EDGAR3.2 1995 distribution in many regions, but is much lower in Europe (by about a factor of 2), slightly lower in east Asia, and lower in north Africa and Chile. This industrial emission is about 10 TgS yr^{-1} lower than the GEIA 1985 emission used in the work of K99. The SO_2 emission from continuous volcanic venting are based on the GEIA volcanic emissions [*Andres and Kasgnoc*, 1998]; however, these are augmented by a factor of 1.5 according to the estimates for quiescent degassing from, e.g., *Halmer et al.* [2002] and *Graf et al.* [1997]. The SO_2 emissions from biomass burning and aircraft are the same as in the work of K99. We assume that 2.5% of all SO_2 emissions are emitted as particulate sulfate.

[20] Our sea-salt production is from the windspeed-dependent formulation for sea-salt generation from whitecap

Table 1. Global Annual Sulfur Budgets

Parameter	Value
<i>DMS</i>	
Source/sink, Tg S yr ⁻¹	
Emission/chem sink	21.2
Burden, Tg S	0.15
Lifetime, days	2.6
<i>MSA</i>	
Sources, Tg S yr ⁻¹	
DMS oxidation	1.8
Sinks, Tg S yr ⁻¹	
Dry deposition	-0.3
Wet deposition	-1.5
Burden, Tg S	0.04
Lifetime, days	8.6
<i>SO₂</i>	
Sources, Tg S yr ⁻¹	85.2
Industrial emissions	52.9
Volcanic emissions	10.7
Photochemistry	19.4
Biomass burning	2.3
Sinks, Tg S yr ⁻¹	
Dry deposition	-48.5
Aqueous phase	-15.2
Wet deposition	-10.5
Gas phase	-11.0
Burden, Tg S	0.66
Lifetime, days	2.8
<i>Sulfate</i>	
Sources, Tg S yr ⁻¹	27.6
Direct emissions	1.7
Gas phase	11.0
Aqueous phase	15.2
Sinks, Tg S yr ⁻¹	
Dry deposition	-3.2
Wet deposition	-24.7
Burden, Tg S	0.47
Lifetime, days	6.2

bubble bursting by *Monahan et al.* [1986]. We use 2 size bins, having dry submicron size ranges of 0.1–1 μm and 1–4 μm . Hydrated at 80% relative humidity (RH) these ranges are approximately 0.2–2.1 μm and 2.1–8.6 μm , respectively. Model surface winds are used to determine the sea-salt emission.

[21] The source of ^{210}Pb is the decay of gaseous ^{222}Rn (half-life is 3.8 days). There is uncertainty in emission rate so we work with 3 different sources. Since radon is thought to be emitted primarily from nonfrozen soils, most previous model studies [e.g., *Jacob et al.*, 1997; *Rasch et al.*, 2000a; *Liu et al.*, 2001; *Balkanski et al.*, 1993] assumed a fixed emission of 1 atom $\text{cm}^{-2}\text{s}^{-1}$ from nonfrozen land with some reduced emission amount from higher latitudes (north of 60°N) or from frozen land and water. We work with that of B93, which assumes 1 atom $\text{cm}^{-2}\text{s}^{-1}$ for nonfrozen land, and 1/3 atom $\text{cm}^{-2}\text{s}^{-1}$ for frozen land. For nonfrozen oceans and lakes we assume the weak emission of 0.005 atom $\text{cm}^{-2}\text{s}^{-1}$. A second emission, CR02, based on *Conen and Robertson* [2002], applies a reduction factor to the 1 atom $\text{cm}^{-2}\text{s}^{-1}$ north of 30°N that decreases linearly to 0.2 at 70°N and remains at 0.2 north of 70°N. As described in the work of *Conen and Robertson* [2002], this linear reduction was based on the observed reduction in ^{210}Pb

deposition flux with latitude. The hypothesis was that soil composition and/or water table change with latitude, suppressing radon released at higher latitudes. Finally we use the source of *Schery and Wasiolek* [1998] that includes regional and temporal variability. The global mean emission rate from *Schery and Wasiolek* [1998] is 1.6 atoms $\text{cm}^{-2}\text{s}^{-1}$ and results in excessive ^{210}Pb . Since the absolute emission rate is poorly constrained (Steve Schery, personal communication, September, 2004) we arbitrarily reduce the emission by a factor of 0.5. Compared with the other emissions, this modified *Schery and Wasiolek* [1998] (mSW98) has reduced radon emission in the tropics and Southern Hemisphere, but has larger emissions from some of the Northern Hemisphere continents. The annual mean emission for the 3 sources are 2.1, 2.0 and 1.9 GCI yr^{-1} for B93, CR02, and mSW98, respectively.

[22] Lead-210, the decay product of ^{222}Rn , attaches quickly to particles and has a long half-life (22 years) and is removed by wet and dry deposition.

[23] Beryllium-7 is generated by cosmic ray collisions, primarily at higher latitudes in the stratosphere and upper troposphere. It attaches quickly to nearby fine particles, and has a substantial sink due to decay (half-life is 53 days). Our ^7Be source is from the calculated cosmogenic source function of *Masarik and Beer* [1999], assuming a solar activity modulation parameter $\phi = 700$ MeV (roughly average for the past 30 years) and present day geomagnetic field. The resulting mean production rate is about 0.033 atoms $\text{cm}^{-2}\text{s}^{-1}$, which is about 1/2 that used by K96 (*Lal and Peters* [1967]; based on observed production during a solar maximum year). However, the source of *Masarik and Beer* [1999] is in the middle range of previous estimates, which are greater or less by at least a factor of 2.

4. Model Budgets

[24] The annual mean global budgets for the sulfur species are shown in Table 1. The SO_2 burden is larger (0.66 Tg S) than in the work of K99 (0.56 Tg S), and also than other models (a typical range is from 0.25–0.6 Tg S). This can be attributed to a combination of the increased (especially natural) emissions and the DSB. The DSB formulation only permits exposure of a cloud to oxidants if it grows. As a result, the sink of SO_2 from aqueous phase oxidation has now dropped to 1/2 its amount in the work of K99. The total emission is increased by 6% compared with K99, but the natural emission is double that in the work of K99. As we will discuss below, naturally emitted SO_2 tends to have a longer lifetime. Owing to the decrease in aqueous phase sulfate production (with the DSB), our sulfate burden is now less than most (0.47 Tg S; previous studies typically range from 0.55–0.7 Tg S) [e.g., K99; *Rotstayn and Lohmann*, 2002; *Chin et al.*, 2000a; *Barth et al.*, 2000; *Takemura et al.*, 2000]. The sulfate burden in K99 was 0.73 Tg S. The new burdens are similar to those from the DSB simulation in the work of *Koch et al.* [2003].

[25] Making use of a second simulation having natural sulfur emissions only, we find that 53% of the sulfate burden is natural (while 38% of the SO_2 source is natural). There is a considerable range in previous natural sulfate fraction estimates. Those that we know of include 60% [*Chin and Jacob*, 1996], 44% [*Feichter et al.*, 1996], 23%

Table 2. Natural Species Budgets

Parameter	Value
<i>Sea Salt</i>	
Sources, Tg yr ⁻¹	
Emissions	1734.4
Sinks, Tg yr ⁻¹	
Settling	-907.3
Wet deposition	-694.1
Dry deposition	-133.1
Burden, Tg	5.2
Lifetime, days	1.1
²²² Rn ^a	
Source/sink GCi yr ⁻¹	
Soils/decay	2.1
Burden, GCi	0.03
Lifetime, days	5.6
²¹⁰ Pb	
Source KCi yr ⁻¹	
Radon decay	994.9
Sinks, KCi yr ⁻¹	
Wet deposition	-797.9
Dry deposition	-195.1
Decay	-1.5
Burden, KCi	49.1
Lifetime, days	17.4
⁷ Be	
Source MCi yr ⁻¹	
Cosmogenic	21.5
Sinks, MCi yr ⁻¹	
Decay	-15.2
Wet deposition	-5.3
Dry deposition	-0.9
Burden, MCi	3.2
Lifetime, days	54.3

^aFor the B93 simulation.

(K99), and 33% [Chin *et al.*, 2000a]. These results depend on the natural emission fraction, model vertical transport efficiency, and oxidation/deposition efficiencies. Our increased natural emission fraction results primarily from the increased proportion of natural emissions. The DSB also has the greatest impact on low-altitude species and therefore has a greater impact on (removal of) industrially derived sulfur species.

[26] Budgets for sea salt and the radionuclides are in Table 2. Although all aerosols settle, only sea-salt particles are large enough to have significant gravitational settling. Because of this they have a relatively short lifetime. Few global sea-salt models have published their budgets for comparison. Our emission, burden and average lifetime are 1734 Tg yr⁻¹, 5.2 Tg and 1.1 days. Chin *et al.* [2002] had a range of emissions and burdens, all larger than ours: 5800–7500 Tg yr⁻¹ and 8–14 Tg, and a smaller lifetime of 0.6 days. Takemura *et al.* [2000] also had a greater emission, 3500 Tg yr⁻¹, a burden similar to ours, 5.6 Tg, and a smaller lifetime of 0.8 days. Model lifetimes are highly dependent on the size ranges simulated. Chin *et al.* [2002] and Takemura *et al.* [2000] include aerosol bins for particles between 4 and 10 μ m, i.e., larger than we consider. These particles would settle quickly and shorten the lifetime.

[27] The budget for the B93 radon emission is shown in Table 2 (2.1 GCi yr⁻¹). The emissions for the other radon

simulations are similar, 2.0 and 1.9 GCi yr⁻¹ for CR02 and mSW98, respectively. Radon is lost only by decay and has a lifetime of over 5 days. It has time to be transported great distances before it decays to ²¹⁰Pb. As a result, ²¹⁰Pb concentrations are large in the upper troposphere and stratosphere and its average lifetime (17 days) is consequently quite long. This lifetime is greater than estimated by Balkanski *et al.* [1993] (about 9 days), but as we will discuss below, our convective scavenging is not as efficient as in their model. Liu *et al.* [2001] also report a tropospheric ²¹⁰Pb lifetime of 9 days. Their precipitation scavenging is also more efficient than ours (our wet deposition accounts for 80% of loss compared with their 89% loss). Model ⁷Be has a very long lifetime because so much of it resides in the stratosphere and therefore its greatest sink is decay (with half-life 53 days). With the tropospheric sinks, the ⁷Be average lifetime is 54 days.

[28] Owing to the significant impact of the DSB on our results we performed a simulation without the DSB. Similar to Koch *et al.* [2003], we found that the sulfate burden without the DSB is about 40% greater. Other soluble species also have greater burdens. The ²¹⁰Pb burden is 17% greater without the DSB. The MSA burden is about 30% greater. The smaller bin sea-salt burden is about 50% greater. The size of the impact depends upon proximity to stratiform clouds. Since sea salt is formed below clouds in the marine boundary layer, the DSB has an especially great impact. The impact on sulfate is also enhanced because of the aqueous sulfate production: a greater portion of the sulfate made in-cloud gets scavenged because of the DSB. Among our species, SO₂ burden is the only one that increases with the DSB. This is because without the DSB formulation, the cloud removes SO₂, generates sulfate and releases sulfate (but not SO₂) at each cloud time step. With the DSB formulation, the cloud does not consume SO₂ at every time step, but only as the cloud grows. Thus the transformation of SO₂ within the cloud causes its behavior to differ from other species.

5. Comparison With Observations

5.1. Radon

[29] We begin with a comparison of our 3 radon emission cases with available radon observations. Of greatest significance are comparison with annual mean surface concentration, and we show these for Mauna Loa (7 years), Gosan (3 years), Hok Tsui (3 years) [Zahorowski *et al.*, 2005], Cape Grim (10 years) (Wlodek Zahorowski, personal communication, September 2004), and Bermuda (Environmental Laboratory web site: <http://www.eml.doe.gov/databases/radon>). These appear in the scatterplot (Figure 1, top) as diamonds (from lowest to highest observed concentrations): Mauna Loa, Bermuda, Cape Grim, Gosan and Hok Tsui. Note that the Mauna Loa observations are high altitude (3400 m) and are only nighttime concentrations in order to avoid up-slope local contamination. We also compare with high altitude aircraft measurements, including those from TROPOZ II (Tropospheric Ozone II) as listed in the work of Mahowald *et al.* [1997] (stars in the upper panel of Figure 1). These measurements were taken near the tropopause (9–11 km) over the oceans at latitudes ranging from 52°S to Greenland, during January and February. We use

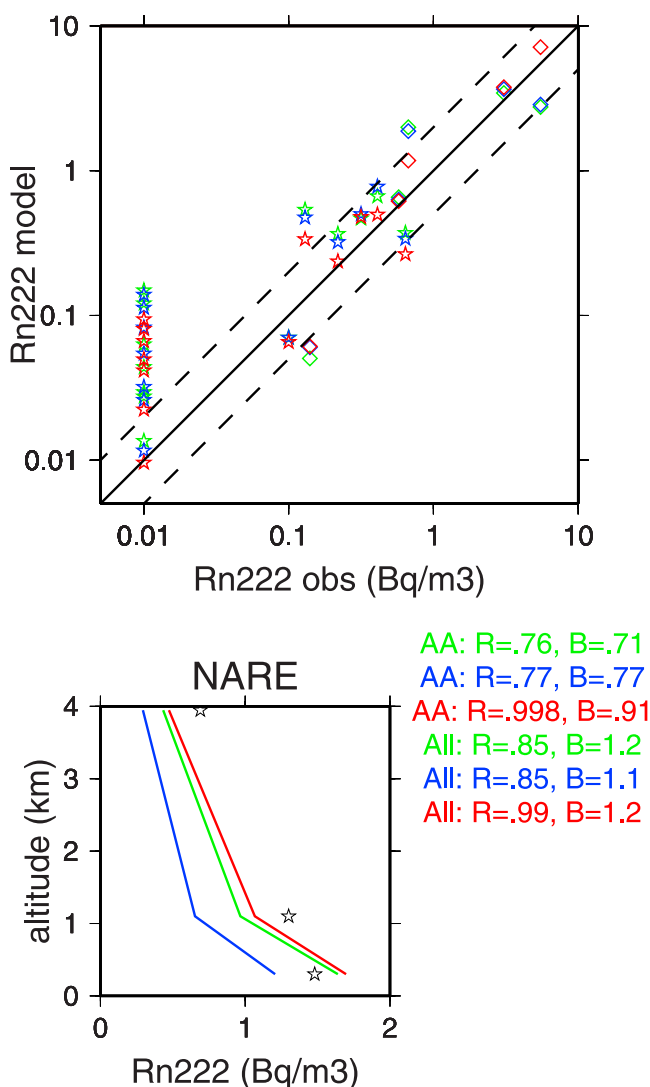


Figure 1. Comparison of radon from the three emission cases (mSW is red; CR02 is blue; B93 is green) with observations. In the upper panel, diamonds are annual mean surface concentrations and stars are aircraft (the observations at 0.01 from TROPOZ are below detection limit). The lower panel shows the profile from the NARE campaign; black stars are the observations where we have binned the data and corresponding model values into 0–600, 600–1600, and 1600–6300 m. Dashed lines show factor of 2. Correlation coefficient, R , and bias, B (defined as the average ratio of model to observation), are given for the annual average data (AA) and for all points (All).

the model mean value from January and February at the corresponding grid boxes. The lower panel shows comparison with aircraft observations from the North Atlantic Regional Experiment (NARE), near Nova Scotia in August. In general, based on this very small database, all 3 emissions give radon surface concentrations that are less than observed but if we include the high-altitude observations, the bias is high. This suggests that the model tends to have somewhat excessive vertical transport. Note that the correlation is best for mSW98 (in red), which is encouraging due

to the care taken in this inventory to capture regional variability.

5.2. Annual Mean Surface Concentrations

[30] Next we compare the model with annual mean surface concentrations, beginning with the natural species and then considering the pollution-impacted sulfur species.

[31] Figures 2 and 3 show the ^{210}Pb and ^7Be annual mean surface concentration and comparison with measurements. The data are primarily from the Environmental Measurements Laboratory (EML) (references are in K96) with duration between 2 and 25 years. The ^7Be data are corrected to a mean solar year, as described in K96.

[32] In Figure 2 (lowest three panels) we show the layer 1 ^{210}Pb concentrations from the 3 radon emission simulations. The ^{210}Pb surface concentrations are maximum close to their (continental) source regions and decrease over the oceans and in the Southern Hemisphere. Of the simulations, mSW98 has the highest concentrations over the NH continents and in the Arctic but the lowest concentrations in the tropics and SH. All 3 simulations generally have high bias relative to the observations. Defining bias, B , as the average ratio between model and observations then $B = 2.2$, 2 and 2.2 for B93, CR02 and mSW98, respectively. The respective correlations are $R = 0.65$, 0.72, and 0.68. Thus the performance of the 3 cases are not very distinct. We show the scatter and bias distribution for CR02 in Figure 1. Since the B93 model includes reduction of the radon emission (by 1/3) for frozen soil, we also performed a simulation of CR02 with reduced flux from frozen soils. This further reduced the high-latitude concentrations and gave better agreement in Figure 1 (the annual mean concentrations); however, it gave very poor seasonality, as we will discuss below. Our ^{210}Pb model seems to do a better job capturing the observed magnitudes in remote regions, such as oceanic islands and the Arctic, compared with previous models as summarized in the work of *Barrie et al.* [2001]. Most of these had ^{210}Pb in excess by a factor of 2 in these remote regions.

[33] Beryllium-7 is generated primarily at high latitudes of the stratosphere and upper troposphere. Stratosphere-troposphere exchange, which is maximum at middle to high latitudes during springtime, brings ^7Be into the troposphere. Convective transport, generally maximum in summertime, is the primary mechanism to transport ^7Be to the surface. Thus all these model processes have important impacts on ^7Be . Our previous simulation, K96, used a very early version of the GISS model that lacked convective cloud entrainment. Without entrainment, ^7Be was delivered from high altitudes to the surface by convective subsidence without undergoing scavenging. This resulted in very large model ^7Be biases in the tropics (about 50% excess) and over continents during summertime. The current GISS model, with a more sophisticated convective cloud parameterization, now captures the observed decrease in ^7Be at low latitudes. Note that in Figure 3, many of the locations with low bias are located in regions where model precipitation is excessive (shown in Figure 4), such as the south-central Pacific ocean, the northwest coast of South America and the Caribbean.

[34] Both sea salt and DMS are transferred from the sea to the atmosphere by wind-driven mechanisms. While there

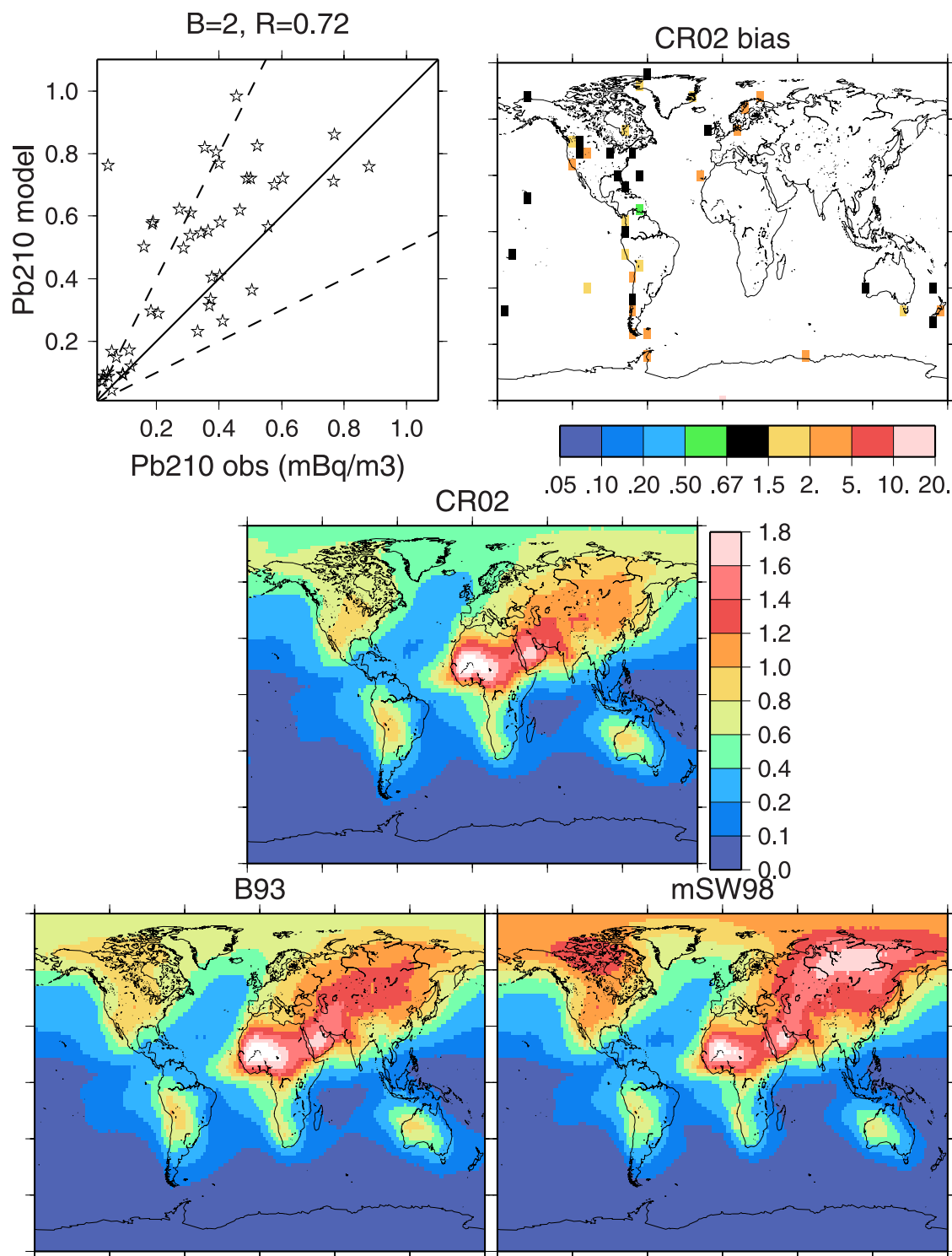


Figure 2. The bottom three panels are ^{210}Pb bottom layer concentrations for the three radon emissions. The top two panels are a scatterplot of surface concentrations for CR02 model versus observations and the CR02 bias (ratio model/observations) in map view. Units are mBq m^{-3} .

are few data for DMS, data are abundant for its particulate oxidation product MSA. In Figures 5 and 6 we compare sea salt and MSA annual mean model surface concentrations with observations (from D. Savoie and J. Prospero, personal communication, November 1999). The observations are from the 1980–1990s with the exact dates varying among

sites. The surface concentration distributions are similar for these species with wind-driven sources. MSA is higher compared to sea salt over continents since its DMS precursor can be transported some distance prior to being oxidized. The model sea salt and MSA are both excessive near Antarctica where the ocean expanse is large and winds are

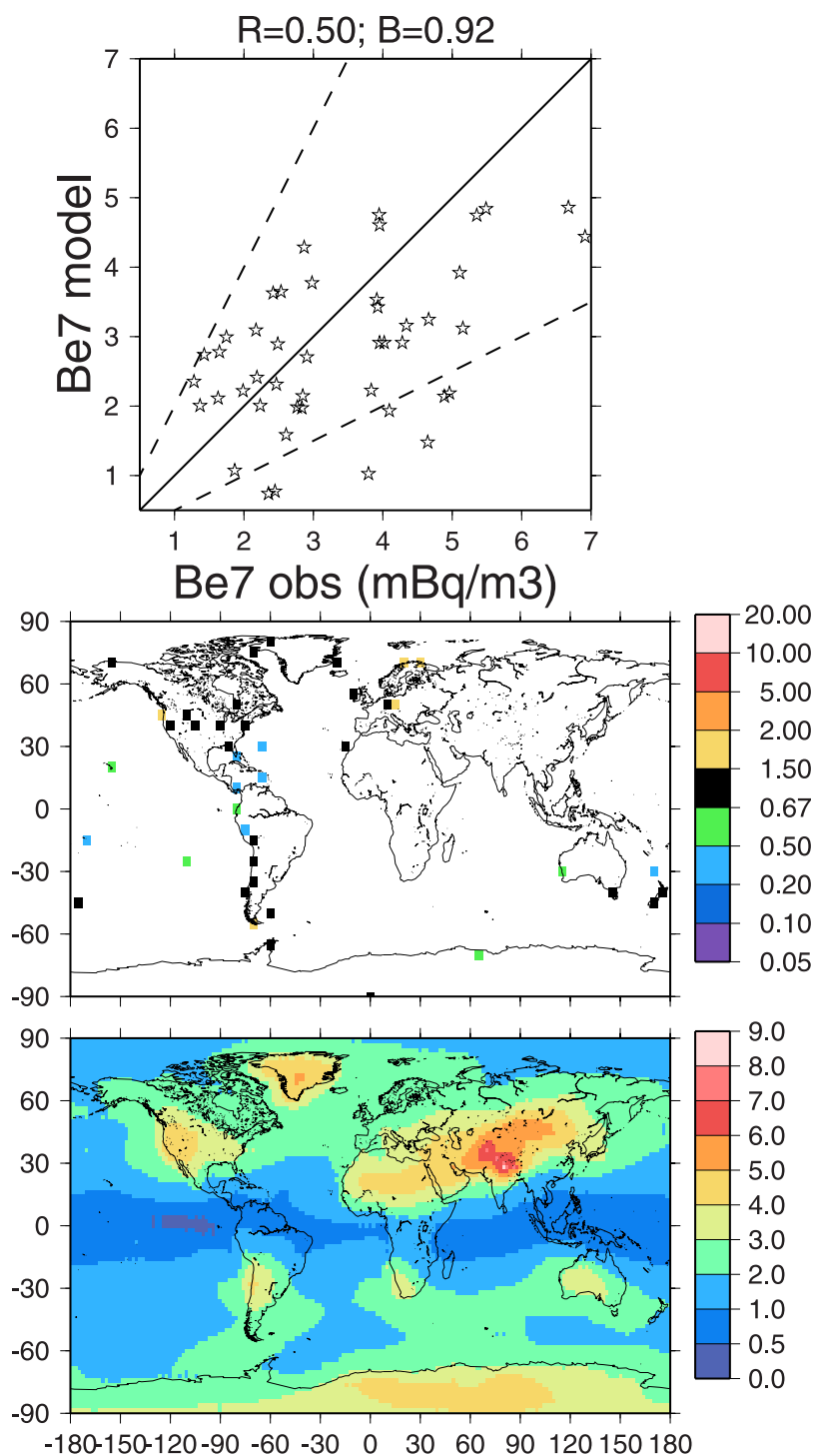


Figure 3. Scatterplot of observed and modeled ^7Be annual mean surface concentrations (top), model bias (ratio between modeled and observed concentrations) (middle), and the model surface concentration (bottom). Units are mBq m^{-3} .

strong. The model DMS is also excessive in this region. At Cape Grim (38S 78E), model DMS is excessive by a factor of 1.5; model SO_2 is excessive by a factor of 2.2. At Amsterdam Island (40S 144E) model DMS and sulfate are both excessive by a factor of 2.7. (See K99 for these observation references.) Outside the windy southern oceans, the model MSA generally agrees with observations to

within a factor of 2. However, outside the windy southern oceans, sea salt tends to be deficient. This may be due to our lack of large sized particles (above 4 μm dry radius), while the observations have essentially no upper size limit (D. Savoie, personal communication, November 1999). Note also that many of the locations where sea salt is deficient coincide with regions where the model precipitation is

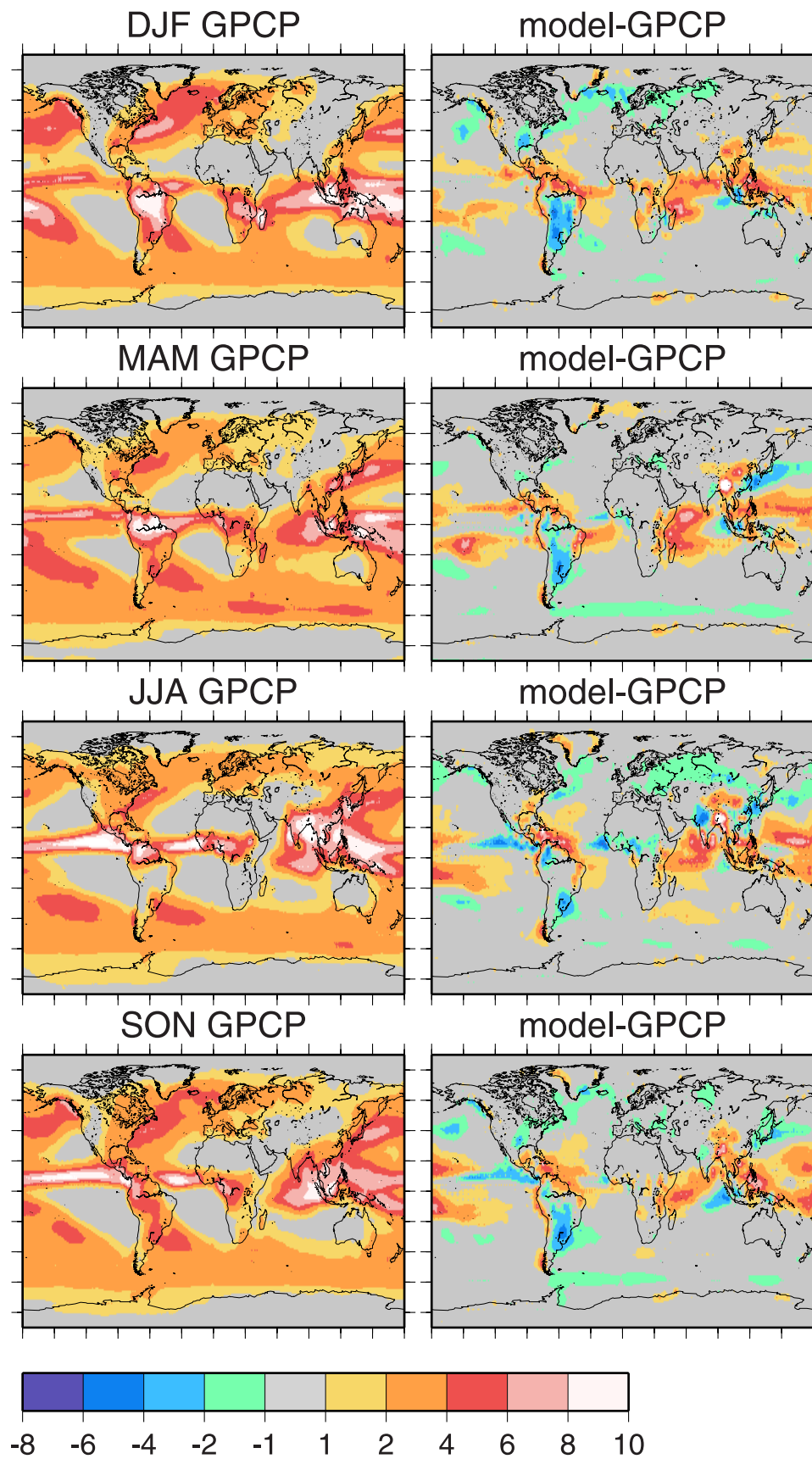


Figure 4. Observed precipitation (Global Precipitation Climatology Project, 1987–1998) and difference between modeled and observed precipitation (mm day^{-1}) for each season.

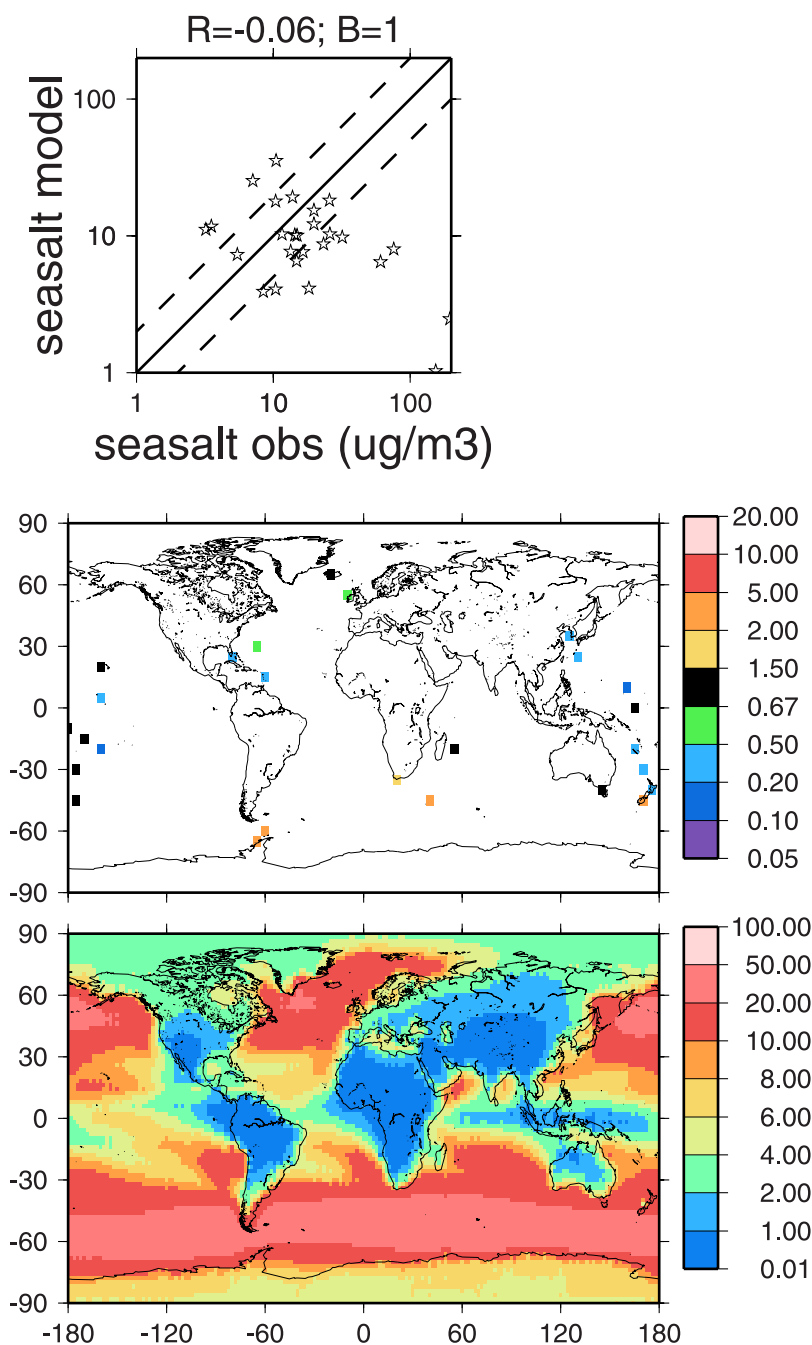


Figure 5. Scatterplot of observed and modeled sea salt annual mean surface concentrations (top), ratio between modeled and observed concentrations shown a map (middle), and the model surface concentration (bottom). Units are $\mu\text{g m}^{-3}$.

excessive (e.g., low latitudes of the western Pacific; see Figure 4).

[35] Next we consider the sulfate distribution. It is interesting to compare the surface sulfate and ^{210}Pb distributions. Both species have a gaseous precursor originating primarily from continents. Sulfate peaks near anthropogenic source regions. Sulfate is lower in the Arctic since its production depends upon the availability of photo-oxidants. Both have substantial concentrations over dry north Africa.

[36] Annual mean model sulfate is compared with observations in Figure 7 in oceanic regions, Europe and the United States. The oceanic data are from the Savoie and Prospero data set (see above). The European data are from the co-operative programme for monitoring and evaluation of the long-range transmissions of air pollutants in Europe (EMEP) for 1995–2001. We use 112 European sites that have more than 7 months of observations in at least one year. The U.S. data are from the Interagency Monitoring of Protected Visual Environments (IMPROVE) network. We

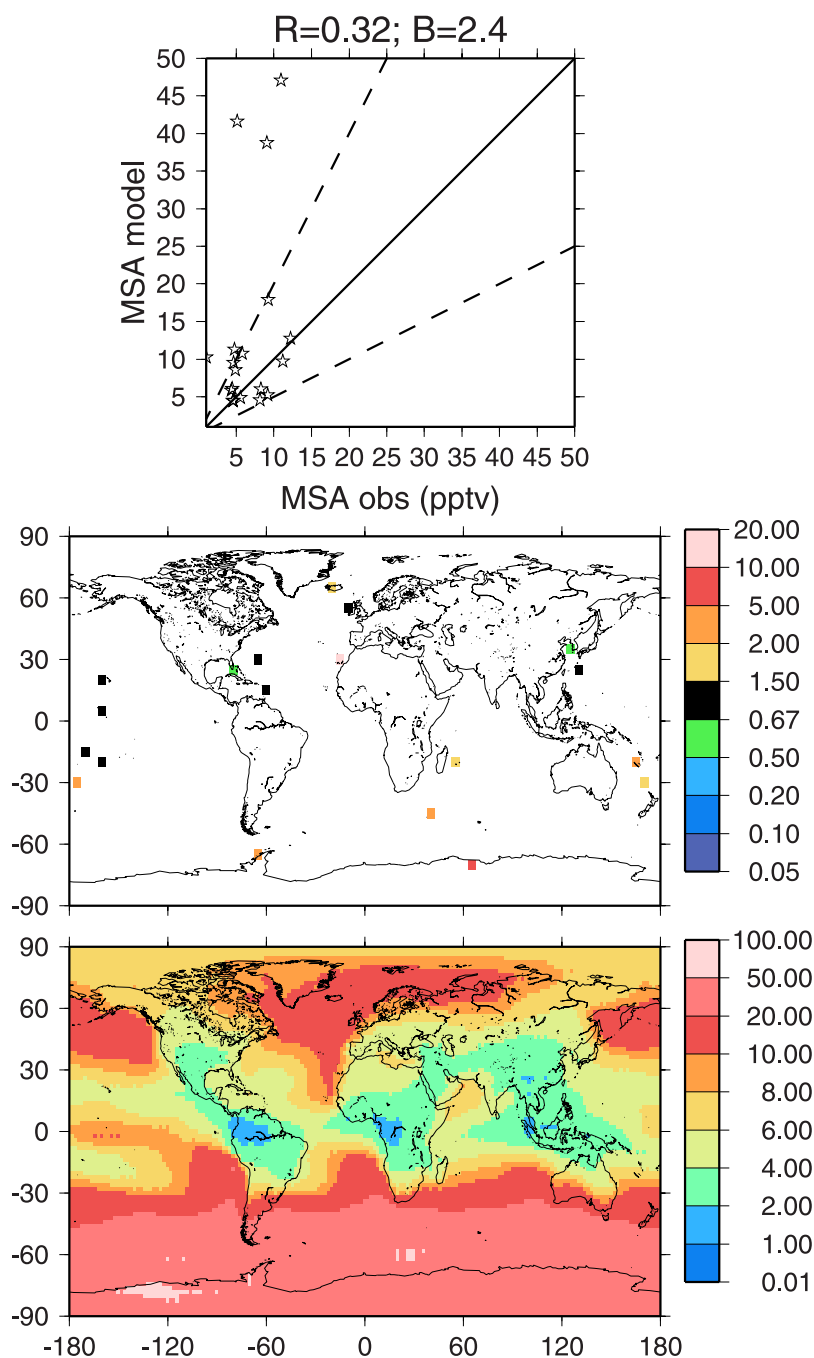


Figure 6. Scatterplot of observed and modeled MSA annual mean surface concentrations (top), ratio between modeled and observed concentrations shown a map (middle), and the model surface concentration (bottom). Units are pptv.

use the 88 sites with at least 7 months of data per year for at least 3 years between the years 1995 and 2003.

[37] Sulfate over oceanic regions comes mostly from the natural DMS source and is less than observed, with an average model bias of 0.54. The bias is only slightly higher than in K99 (which had a bias of about 0.47), in spite of the increased DMS production used here. Other DMS oxidant products (MSA and SO_2) in remote regions have increased in this model version. The sulfate bias appears to be a result of the decreased sulfate in the DSB formulation.

[38] In Europe, sulfate is also less than observed ($B = 0.58$). Europe has excessive model SO_2 , with an average bias of 5 (not shown). The previous model (K99), which used the GEIA 1985 emissions, also had a positive SO_2 bias (about 1.75) and a low sulfate bias (about 0.7). As we will show in the following section, the bias is worst during winter when oxidants at high latitudes are limited. These difficulties simulating the sulfur cycle are common in global models [e.g., *Barrie et al.*, 2001; *Chin et al.*, 2000b] and some have suggested the need for additional oxidation

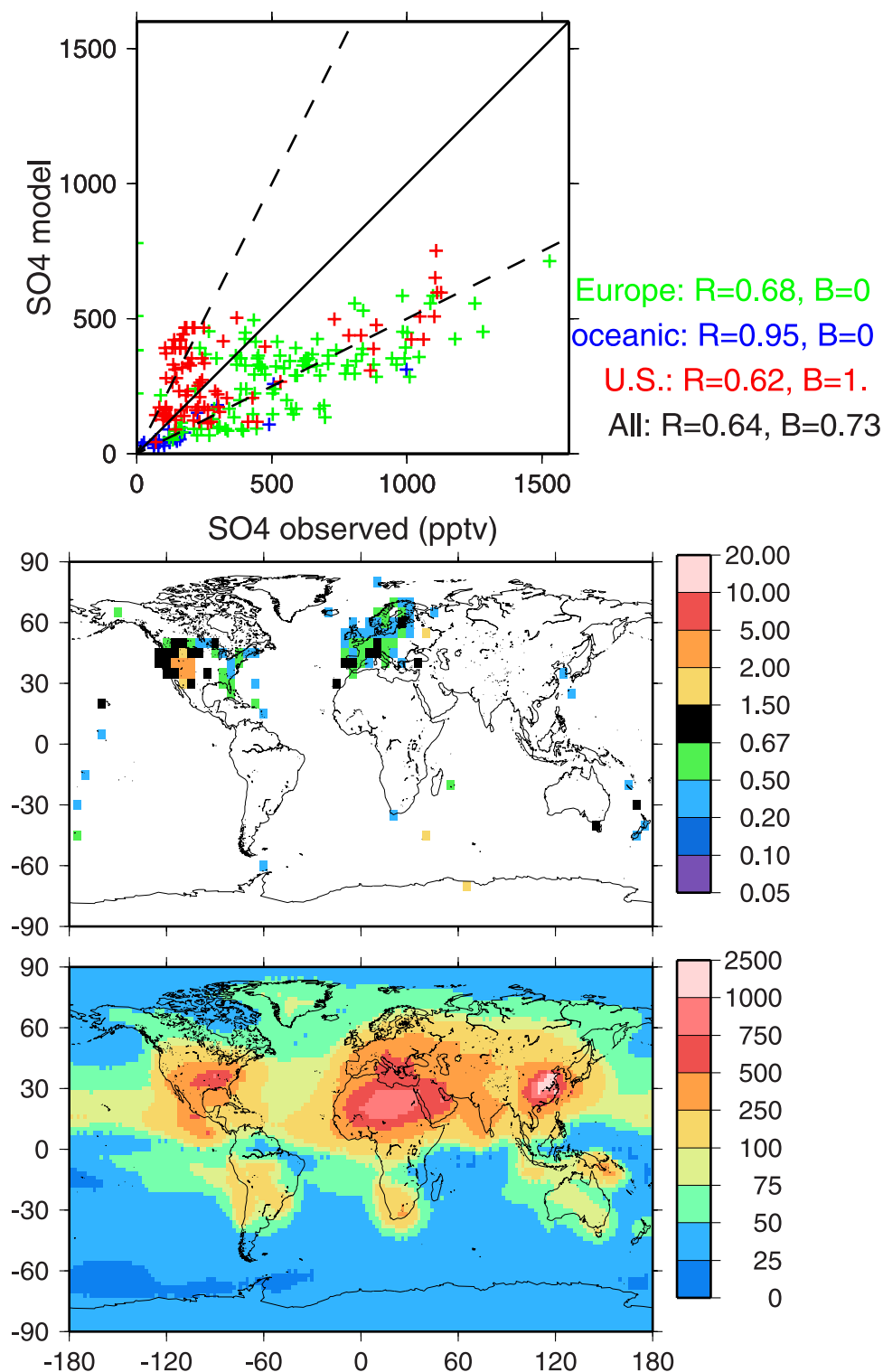


Figure 7. Scatterplot of observed and modeled sulfate annual mean surface concentrations for remote sites (blue), Europe (green), and United States (red) (top); ratio of model to observed concentrations (middle); and the model surface concentration (bottom). Units are pptv.

mechanisms. Perhaps more noteworthy are the few models that do not have high SO_2 bias in Europe, such as *Barth et al.* [2000], *Rotstajn and Lohmann* [2002] and *Berglen et al.* [2004]. These models include aqueous-phase oxidation by ozone and that helps reduce SO_2 concentrations in Europe.

In a companion paper [*Bauer and Koch*, 2005], we show that adding heterogeneous sulfate formation on dust does boost sulfate production in some regions. Over Europe, the sulfate amount increases by about 50% by this mechanism. The IIASA SO_2 emissions used here are much lower than

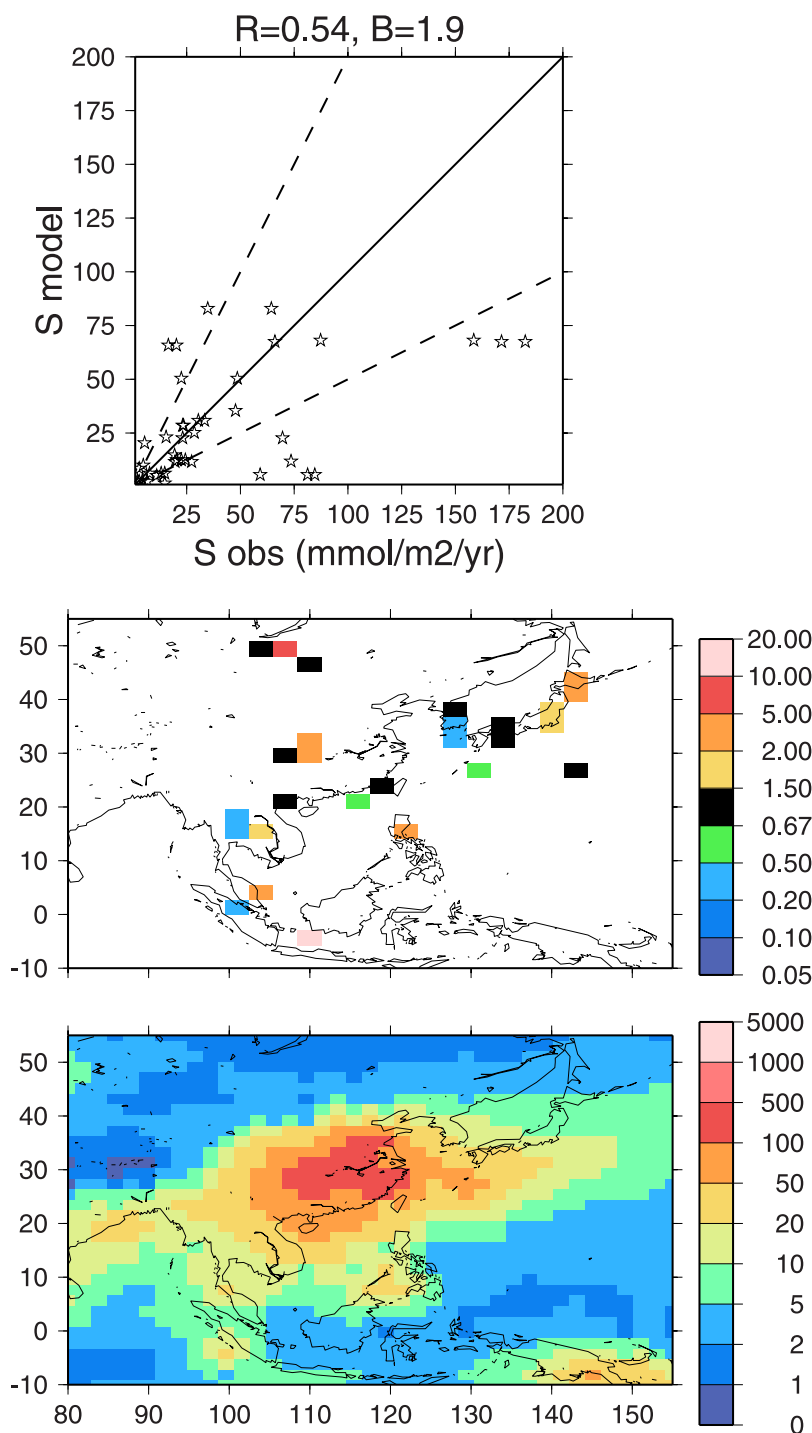


Figure 8. Scatterplot of observed and modeled sulfur deposition (from EANET) annual mean surface concentrations (top), ratio of model and observed deposition flux (middle), and the model deposition flux (bottom). Sites within a 3×3 degree grid box are averaged together. Units are $\text{mmol m}^{-2} \text{yr}^{-1}$.

other emission estimates over Europe. We have also used the EDGAR (v2.3) 1995 emission. Over Europe, the bias using EDGAR is improved (0.68); however, the correlation is worse (0.33) and the SO_2 bias is even higher ($B = 8$).

[39] Over the United States the model bias tends to be low in the polluted eastern seaboard region and high over the Rocky Mountains. These biases occur primarily during the summertime. Thus it appears that sulfate produced most

heavily in the east tends to be advected westward rather than being confined to its production region. This may be related to low mean mountain topography at the relatively coarse model resolution used here.

[40] A third major source region is Asia where long-term surface concentration data are not readily available. In Figure 8 we compare model sulfur deposition data from the Acid Deposition Monitoring Network in East Asia

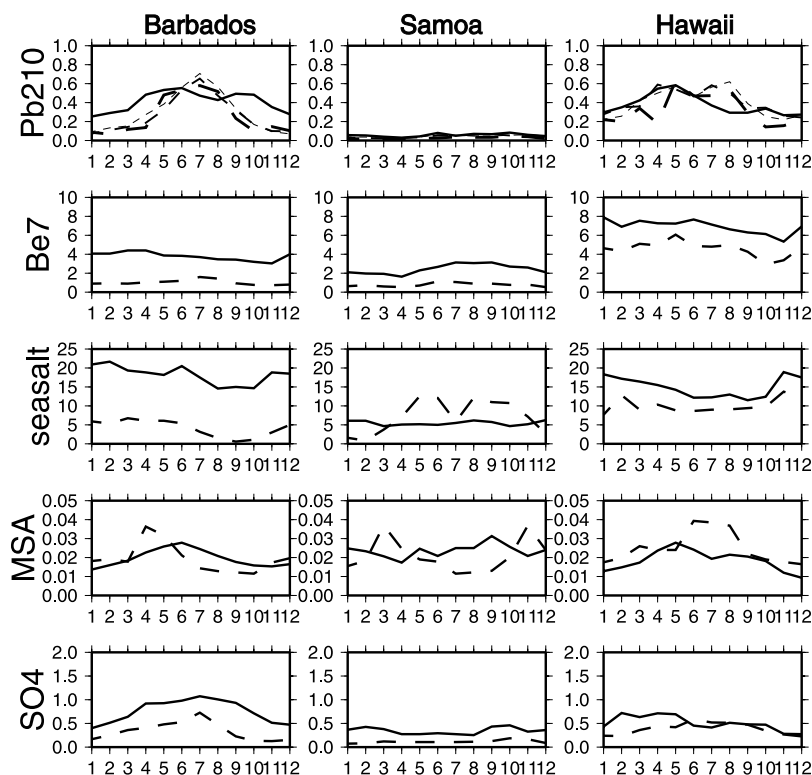


Figure 9. Seasonality observed (solid) and modeled (dashed) for aerosol species at low-latitude oceanic stations. The radionuclides have unit mBq/SCM, and all others have units $\mu\text{g}/\text{SCM}$. The radionuclide observations at Hawaii are from Mauna Loa at 3400 m, while the others are from Oahu close to sea level. The ^{210}Pb model results are shown for B93 (fine dashed line), CR02 (medium dashed line), and mSW98 (fat dashed line).

(EANET) for the years 2000–2001. We note that deposition data have very large interannual variability, limiting the usefulness of this short term data set. There is considerable scatter in the comparison and the overall model bias is high.

5.3. Comparison With Observed Seasonalities

[41] Now we consider seasonal variability at various regions for all species, co-located as much as possible. In Figure 9 we show seasonalities for 3 low-latitude oceanic sites. Barbados is observed to have maximum summertime concentrations for ^{210}Pb , MSA and sulfate and slightly peaked wintertime sea-salt concentrations. Overall the model captures these seasonalities. Similarly, Hawaii is observed to have a springtime peak and a secondary fall peak for ^{210}Pb , MSA and sulfate. The wintertime sea-salt maximum is due to increased winds. A slight springtime ^7Be maximum results from increased stratosphere-troposphere exchange. The model biases are mostly without seasonal variation in this region. Model precipitation at Samoa is excessive (see Figure 4) resulting in low model bias. The model sea salt at Samoa is too high in wintertime, similar to sites further to the south in the SH. The model of *Takemura et al.* [2000] was more successful at simulating the sea-salt amount at Barbados; however, their observations are lower than ours, perhaps based on different years.

[42] Seasonality at some high-latitude locations is shown in Figure 10. All (coastal) Antarctic species are observed to have maximum summertime concentrations. Transport from lower latitudes is maximum in summer, carrying ^{210}Pb .

Beryllium-7 also has maximum descent in summer. DMS (and MSA and sulfate) are also highest in summer when DMS water concentrations peak. The model fails to capture this seasonality. The model has too much wintertime ^{210}Pb , associated with excess values over the SH continents throughout the year. Since mSW98 has lower emissions in the SH it has the lowest bias. Previous ^{210}Pb models [*Rasch et al.*, 2000a] suffered from the same seasonal bias, but had lower magnitude. *Liu et al.* [2001] found improved radionuclide simulation at the South Pole when they did not suppress scavenging by frozen precipitation. This suggests that we may not be scavenging adequately in these extreme winter conditions. Our model fails to produce the peak in summertime ^7Be at the coastal Antarctic sites; however, it is more successful at the 2800 m South Pole station (not shown). As already discussed, the wind-derived species are excessive near Antarctica. Here we see that the MSA bias occurs mostly in summertime during the DMS bloom, while the sea-salt bias is greater in winter when the winds are stronger. Antarctic sulfate, primarily derived from DMS, agrees with the observations (due to the low in-cloud sulfate production as discussed above).

[43] In the Arctic, ^{210}Pb , ^7Be and sulfate are carried poleward during the late winter/early spring “Arctic haze” transport. As in the south, sea-salt generation is maximum in the windy winter and MSA is maximum in the summer. The model is much more successful for these wind-derived species in the NH. This may be because the overall production is larger in the southern oceans, due to the larger

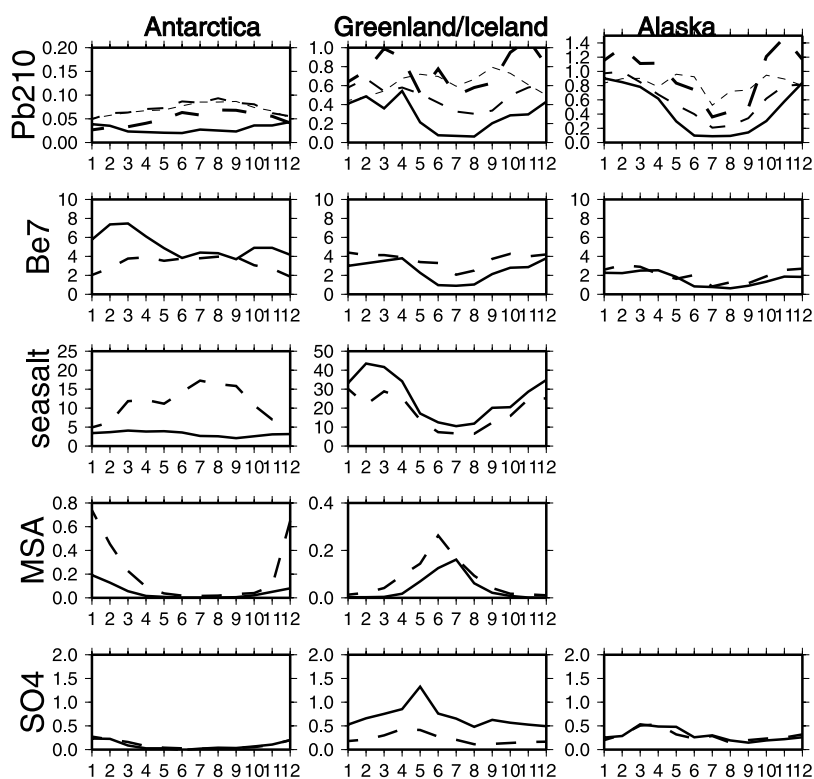


Figure 10. Seasonality observed (solid line) and modeled (dashed line) at high-latitude remote stations. In Antarctica the radionuclides are from Mawson; the rest are from Palmer. In Greenland/Iceland the radionuclides are from Kap Tobin, and the rest are from Heimaey. In Alaska the radionuclides are from Barrow, and sulfate is from Denali National Park. The radionuclides have units of mBq/SCM, and all others have units of $\mu\text{g}/\text{SCM}$. The ^{210}Pb model results are shown for B93 (fine dashed line), CR02 (medium dashed line) and mSW98 (fat dashed line).

expanse of open ocean, together with the long lifetimes of species in our model [Textor *et al.*, 2005]. The model ^7Be is quite successful, and improves upon the previous models of K96 and Land and Feichter [2003] which were unable to attain the observed winter-springtime ^7Be levels. The Arctic is perhaps the regions where the 3 radon emission simulations differ most. The B93 simulation gives poor ^{210}Pb seasonality since wintertime radon emission is excessively suppressed by the frozen-soil parameterization. Lead-210 from mSW98 has good seasonality but is too large. CR98 is most successful; however, had we suppressed the frozen-soil emissions the seasonality would have been poor (i.e., wintertime ^{210}Pb would have been too small). This comparison suggests that the radon emissions should not be suppressed for frozen soils and that the high-latitude reduction in radon emissions is due primarily to other mechanisms. Our positive ^{210}Pb bias in the Arctic contrasts with previous models, that tended to underestimate the magnitude there [Rasch *et al.*, 2000a; Liu *et al.*, 2001]. Sulfate seasonality is well simulated and the magnitude at Alaska is excellent; the magnitude in Greenland is less than observed. Some models have reported difficulty with deficient amount and poor sulfate seasonality in the Arctic [e.g., Barth *et al.*, 2000; Rotstajn and Lohmann, 2002]. Our success may be due to the model's relatively efficient poleward low-altitude transport compared with other models [Textor *et al.*, 2005].

[44] Figure 11 shows seasonality in Europe. There is a slight tendency for ^{210}Pb to peak in winter and ^7Be in summer over central Europe (e.g., Germany). The model has excessive ^{210}Pb in summertime. Note that the model ^7Be seasonality in Norway resembles that in Greenland, with peak winter values, but the observations are flat. Both radionuclides are transported from the south to Norway (note their similar seasonalities). The excessive wintertime values may be due to deficient model precipitation in northwestern Eurasia during winter (Figure 4). Here again we see large differences among the radon emission scenarios, with the greatest wintertime excess resulting from the mSW98 emission.

[45] The sulfur species vary considerably in magnitude across Europe and even within grid boxes, as we demonstrate by showing data from multiple sites when located within a single model grid box. The model performance varies across Europe as well, so these 5 grid boxes are a small sample. In general, SO_2 is maximum in winter, which the model simulates but in great excess. The model sometimes has greater wintertime bias (relative to summertime) (as in Russia) and sometimes not (as in Germany). In general the wintertime bias is greater for the more polluted regions. Observed sulfate seasonality is sometimes flat, sometimes peaks in winter and sometimes in summer. There are few regional tendencies in seasonalities, except perhaps

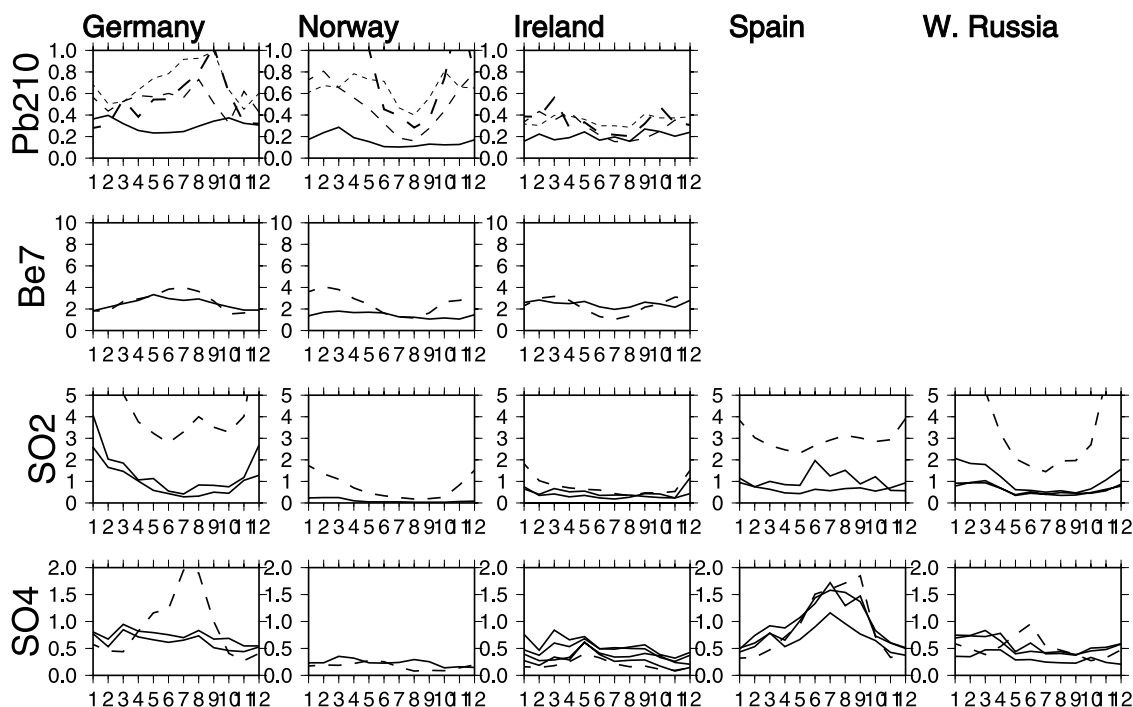


Figure 11. Seasonality of observed (solid line) and modeled (dashed line) in Europe. All (EMEP) sites within a model grid box are shown. The German data are from Braunschweig (radionuclides) and from Brotjackriegel and Schmucke (sulfur species). The data in Norway are from Skibotn (radionuclides) and from Tustervatn (sulfur species). The data in Ireland are from Mace Head (radionuclides), and from Lough Navar (Great Britain), Turlough Hill, The Burren, and Ridge of Capard (sulfur species). The data in Spain are from San Pablo de los Montes, Zarra and Viznar. The data in Russia are from Shepeljovo, Lahemaa (Estonia), and Zoseni (Latvia). The radionuclides have units of mBq/SCM, and the sulfur species have units of $\mu\text{g}/\text{SCM}$. The ^{210}Pb model results are shown for B93 (fine dashed line), CR02 (medium dashed line), and mSW98 (fat dashed line).

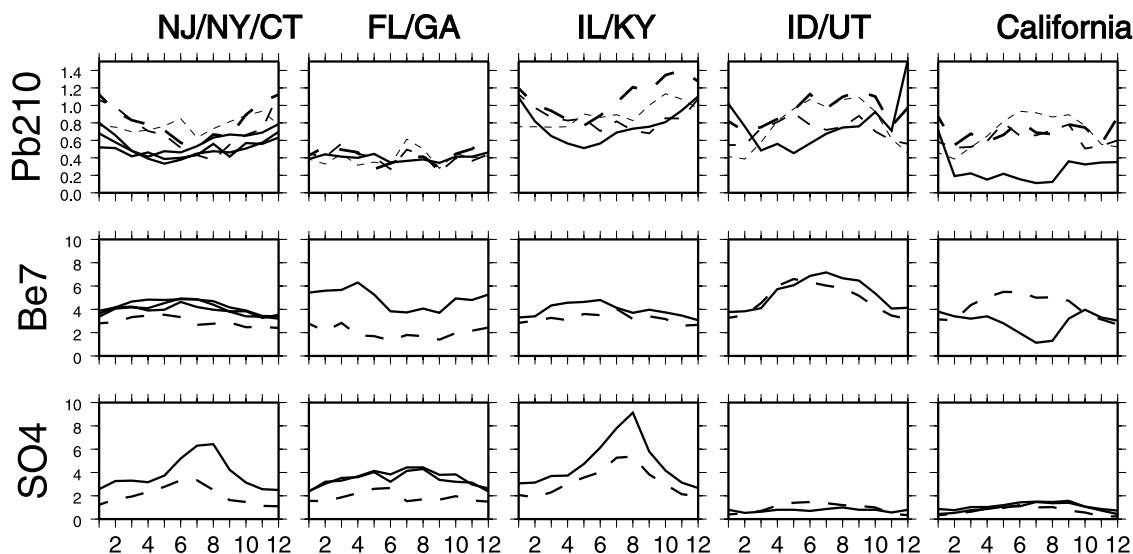


Figure 12. Seasonality of observed (solid line) and modeled (dashed line) in the United States. All sites within a model grid box are shown. The radionuclides have units of mBq/SCM, and the sulfur species have units of $\mu\text{g}/\text{SCM}$. The ^{210}Pb model results are shown for B93 (fine dashed line), CR02 (medium dashed line), and mSW98 (fat dashed line).

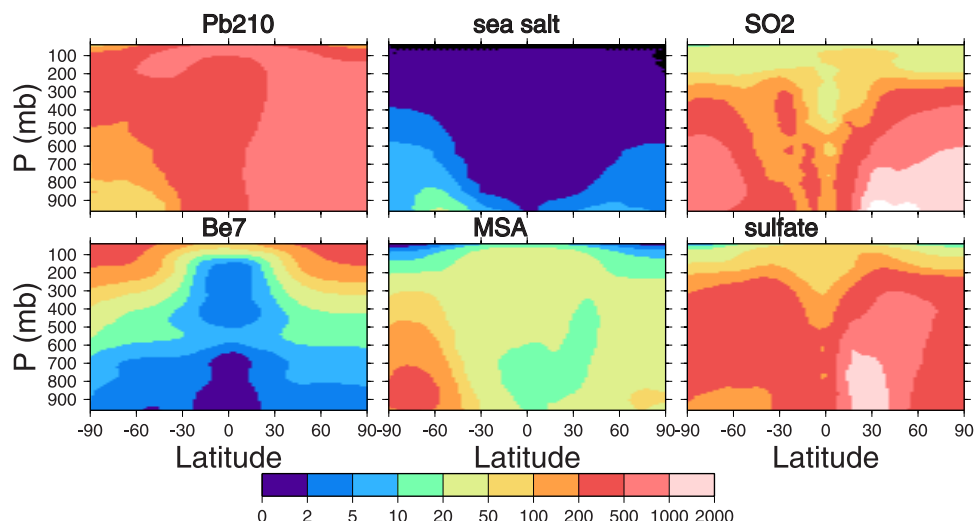


Figure 13. Annual, zonal mean concentrations. Units are mBq/SCM for ^7Be , $\mu\text{Bq/SCM}$ for ^{210}Pb , ng/SCM for the sulfur species, and pg/SCM for sea salt.

for a summertime peak in southern Europe (e.g., Spain). The model sulfate generally peaks in summertime over Europe (e.g., Spain, Germany), but not everywhere (Ireland, Russia). This summertime peak is often lacking in the observations, so that the model will have either a positive summertime bias and/or a negative winter bias. Note that ^{210}Pb has a similar positive summertime bias. A low sulfate wintertime bias is common among models [e.g., *Chin et al.*, 2002b; *Barrie et al.*, 2001; *Rotstayn and Lohmann*, 2002]. Such studies have speculated about possible missing wintertime oxidants that would improve the simulations.

[46] Figure 12 shows seasonal variability over the United States, selecting sites in the northeast, the southeast, the midwest, the Rocky Mountain region and the west. We selected grid boxes for sulfate that were close to the available radionuclide data. Over North America (except in Florida), ^{210}Pb peaks in the wintertime when greater boundary layer stability limits dilution of the surface-derived radionuclide. At most sites, mSW98 and CR02 capture the observed seasonality. B93 is less successful since it has too much winter radon emission suppression. Beryllium-7 peaks in summer, except along the west coast and in Florida where summertime precipitation reduces concentrations. The model seasonality is successful other than having excessive ^7Be in summertime in California. These model excesses in coastal California occur because the model grid box is half land, half ocean. The observations are from Richmond, California, which tends to have maritime influences during summer. If we moved one grid box to the west the model would agree well with observations during summer and would be somewhat low during winter, for both radionuclides. Model sulfate seasonality peaks in summertime and is successful, although the magnitude is generally too low in the east and midwest.

5.4. Altitude Dependence: Comparison With Tropospheric Aircraft Observations

[47] Next we consider the vertical variation of our aerosol species and compare with aircraft observations. Zonal

annual mean concentrations are shown in Figure 13 (the 3 radon cases do not differ significantly in the zonal mean). This model version has greater poleward transport of species such as ^{210}Pb , SO_2 and sulfate than previous versions (e.g., K99). The SO_2 concentrations in the Southern Hemisphere are larger in this version because of the increased DMS emissions. In K99 and K96 aerosol concentrations were very small in the tropical upper troposphere. In these earlier model versions convection was by far the dominant means of vertical transport. Since convective scavenging efficiently removes soluble species in the updraft, this results in low concentrations near the tops of the plumes (i.e., especially in the tropical upper troposphere). For (the surface-derived insoluble) DMS, in K99 the ratio of convective vertical transport to vertical transport by the general circulation was about 10–20 in the middle to upper troposphere. In the current model version the ratio is about 3–5, indicating that convection is relatively less important for vertical transport in the current model. Thus the soluble species have increased opportunity to be lofted without getting scavenged.

[48] The best way to check the model's ability to capture vertical variability of individual species is by comparing with aircraft measurements. Such measurements are of brief duration (typically minutes to hours for each measurement, over the course of a several day campaign) and typically campaigns are designed to examine pollution events. However, our comparison with several campaigns shows remarkable consistency lending confidence to the reliability of the data constraint. In Figure 14 we compare the model with aircraft-based profiles, choosing more recent campaigns in order to be consistent with the anthropogenic sulfur emissions. To construct the profiles, we sample the monthly mean model concentration at the same location (grid box) as the aircraft sample. Then we average over all points in a given model level. The campaigns include TRACE-P (March–April 2001 in the Pacific Ocean), PEM-West B (February–March 1994 in the Pacific Ocean), PEM-Tropics A (September 1996 in the tropical Pacific), PEM-Tropics B

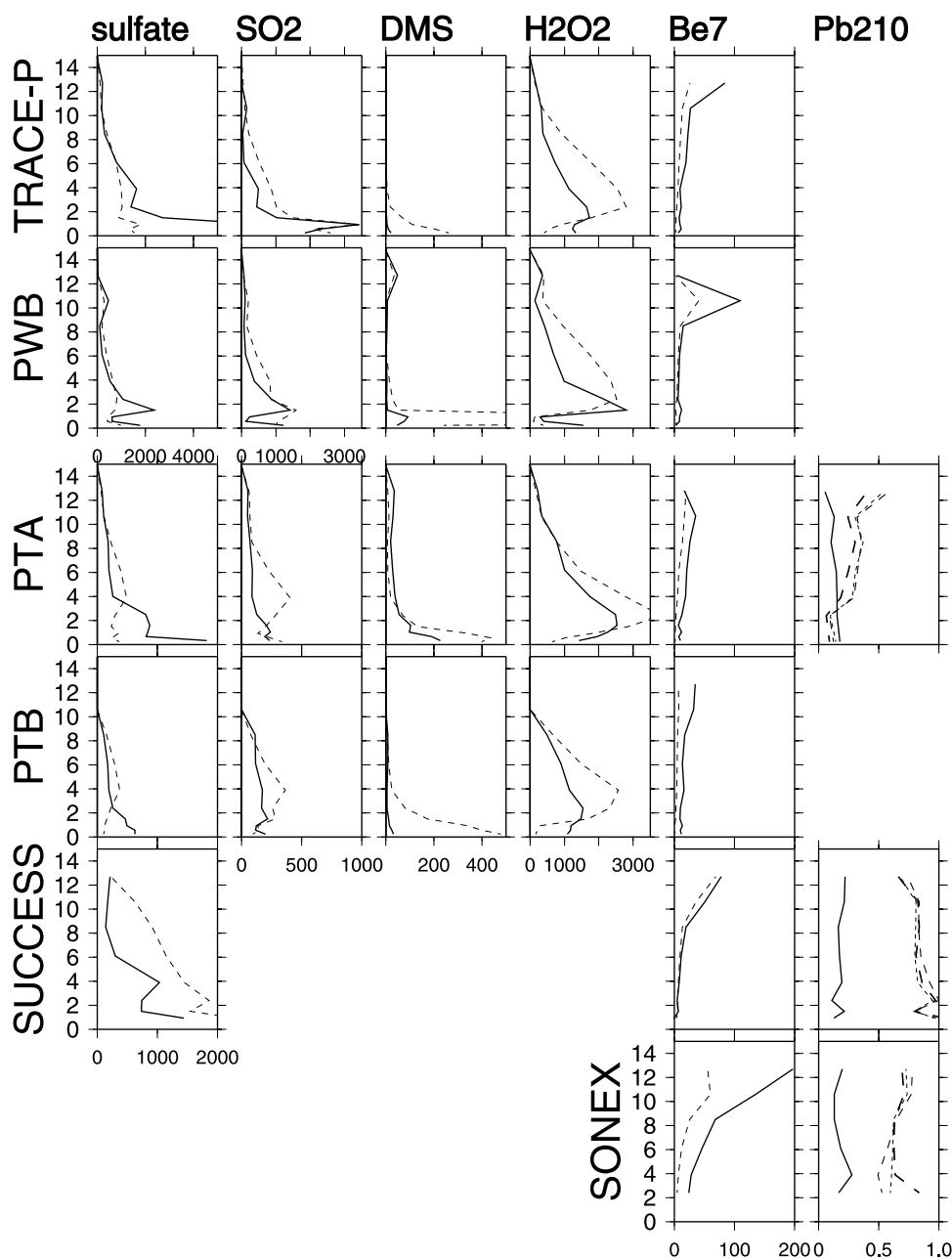


Figure 14. Comparison of model (dashed line) with aircraft (solid line) profiles. The vertical axis is altitude (km). Units are mBq/SCM for the radionuclides and ng/SCM for the other species. Note that the top two rows have different horizontal scales for SO₂ and sulfate. Profiles are constructed by using the model values at the locations corresponding to each observation and then averaging all model and observed values. For TRACE-P, measurements from the DC-8 only are used; for PEM-tropics B, measurements from the P3B only are used except for ⁷Be from the DC-8.

(March–April 1999 in the tropical Pacific), SUCCESS (April 1996 over the United States), and SONEX (October 1997 over the south Atlantic).

[49] Consistent with what we have seen so far, the model sulfate is less than observed over the Pacific, especially in the boundary layer. In the tropics, the model sulfate is slightly excessive in the middle troposphere (PTA, PTB). The model sulfate is quite excessive above the United States (SUCCESS). Sulfur dioxide agrees well with observations in the boundary layer but is too large in the middle

troposphere of the Pacific, explaining the sulfate bias there. Model DMS is overpredicted in the boundary layer (of the Pacific) but quickly diminishes with altitude, as observed. Thus we see that model DMS is too large even at low latitudes. Once again we note that the model DMS bias does not result in excessive sulfate (or SO₂). Model H₂O₂ also tends to be somewhat excessive in the middle troposphere. Model ⁷Be is generally less than observed, failing to achieve the maximum values observed at about 12 km, although the agreement above the United States is excellent

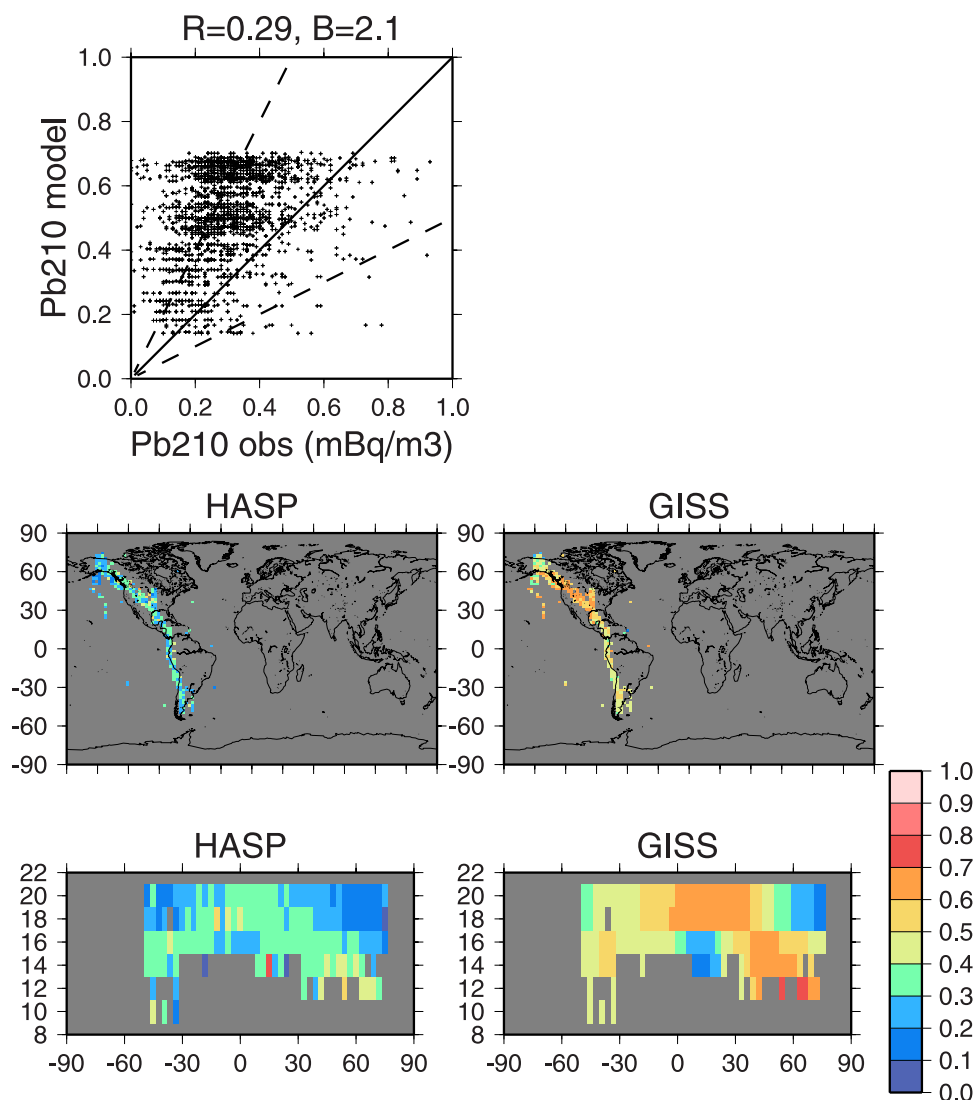


Figure 15. Comparison of EML HASP stratospheric ^{210}Pb aircraft data with (mSW98) model. Monthly mean model values located in grid box corresponding to aircraft measurement are used. All points are shown together regardless of month. The top panel shows a scatterplot comparison of model and observation. Middle panels show map view of observations (HASP) and model (GISS), and bottom panels show zonal averages over observations and model.

(SUCCESS). For aircraft measurements taken near the tropopause [Jordan *et al.*, 2003], the model ^7Be bias is reduced by as much as a factor of 3 if we sample the model in a grid box containing the tropopause. Lead-210 is observed to be fairly uniform with altitude; however, the model ^{210}Pb is much greater than observed, by a factor of 2–4. Liu *et al.* [2001] corrected their excessive midtropospheric ^{210}Pb concentrations by including a cirrus cloud settling parameterization; this reduced their upper tropospheric concentrations by a factor of 2–3. While a similar parameterization might improve our ^{210}Pb it would degrade the other aerosol species (including ^7Be).

[50] Compared with K99, the model sulfate is now increased in the tropics and the sulfate at higher latitudes of the Pacific is decreased (the previous model had too much sulfate in the boundary layer). As shown in the work of Bauer and Koch [2005], heterogeneous production of

sulfate on dust particles dramatically increases the agreement with observations off the coast of Asia (e.g., for PEM-West B and TRACE-P) by removing model SO_2 excesses and generating increased sulfate.

5.5. Altitude Dependence: Radionuclides in the Stratosphere

[51] An extensive database of aircraft stratospheric radionuclide data permit us to examine model processes related to exchange between the stratosphere and troposphere. We use the radionuclide measurements made by the Environmental Measurements Laboratory (EML) High Altitude Sampling Program (HASP) (<http://www.eml.doe.gov/databases/hasp/>). We use over 3200 ^{210}Pb and 3700 ^7Be measurements taken between 1961–1965 and 1970–1983. The location of the measurements is indicated in Figures 15 and 16; they provide good zonal coverage of stratospheric

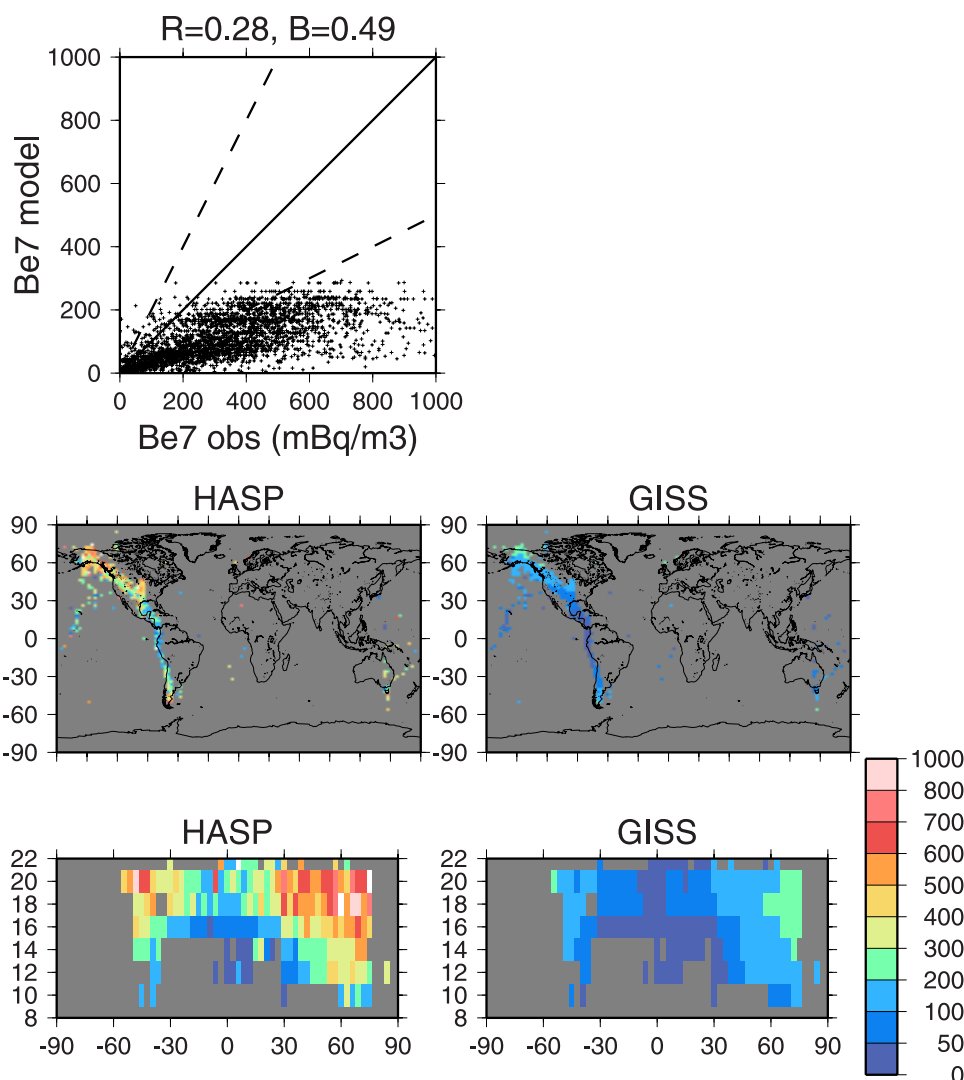


Figure 16. Comparison of EML HASP stratospheric ^7Be aircraft data with model. Monthly mean model values located in grid box corresponding to aircraft measurement are used. All points are shown together regardless of month. The top panel shows scatterplot comparison of model and observation. Middle panels show map view of observations (HASP) and model (GISS), and bottom panels show zonal averages over observations and model.

radionuclide concentrations. We show all measurements, covering various seasons, since we do not expect significant seasonal variability in the stratosphere. Model values are chosen to correspond to the location and month of the measurements. Stratospheric ^{210}Pb is observed to be largest in the lower stratosphere and at higher altitudes of the tropics. Presumably the latter results from tropical pumping of radon and ^{210}Pb into the stratosphere. The maximum ^{210}Pb is seen at NH midlatitudes of the lower stratosphere, above North America. This peak probably results from entrainment of the troposphere into the stratosphere. The model overestimates stratospheric ^{210}Pb nearly everywhere, except perhaps in the tropical lower stratosphere where the model is deficient. The stratospheric results do not differ greatly for the 3 radon simulations. The smallest stratospheric ^{210}Pb results from the mSW98 source, since the tropical radon emissions are least (about 20% lower than the other sources). The stratospheric model bias is consistent

with the excessive free tropospheric ^{210}Pb of the previous section and with the surface concentration bias: all are excessive by about a factor of 2. This bias does not appear to be caused by radon (Figure 1). Thus it appears that either ^{210}Pb is not scavenged near the surface as much as it should be, or that the radon emission is excessive in regions unconstrained by observations.

[52] The model of Liu *et al.* [2001], which used the radon emissions of B93, did not have excessive stratospheric ^{210}Pb . This is probably due to more efficient precipitation scavenging of tropospheric ^{210}Pb , including their parameterization for aerosol sink by cirrus cloud precipitation.

[53] Beryllium-7 has peak production at about 20 km and midlatitudes, as evident in the concentrations shown in Figure 16. Note that the observations span more than a complete solar cycle, so we plot them all together assuming that the source variability will average out.) The model underestimates these peak values, by at least a factor of 2.

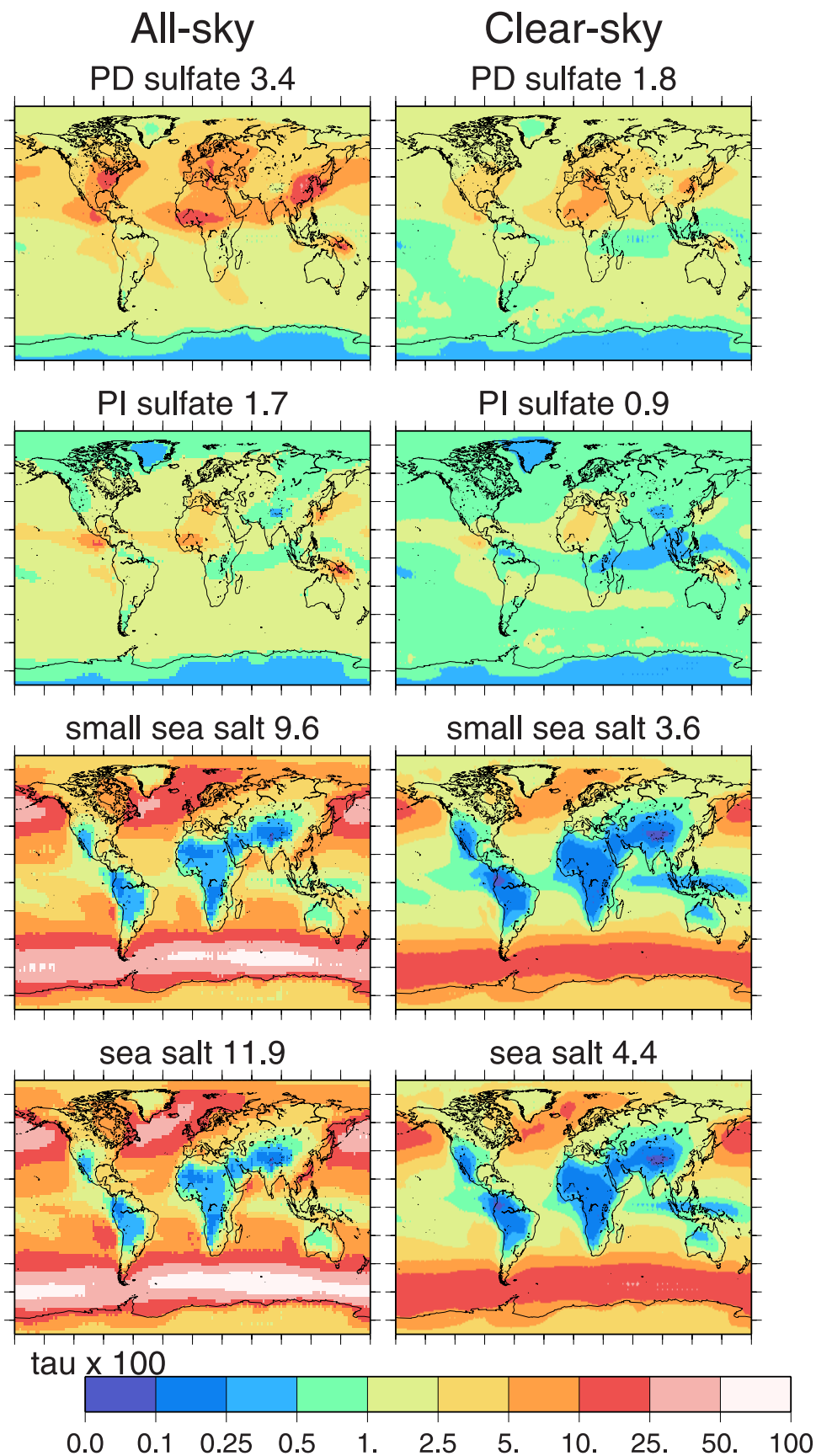


Figure 17. Annual mean optical thicknesses ($\times 100$) for present-day sulfate, preindustrial sulfate, the small-sized sea salt, and total sea salt. The left side is for all-sky and the right for clear-sky only. Mean values for each panel are shown.

As for ^{210}Pb , the stratospheric bias is consistent with the upper tropospheric biases (Figure 14). The stratospheric bias suggests that our source is weak by a factor of 2. Thus the *Lal and Peters* [1967] source, which is larger by a factor of 2, (and used in the work of K96) should correct this bias. Indeed, *Liu et al.* [2001] used the *Lal and Peters* [1967] source and found good agreement with the stratospheric measurements.

6. Aerosol Optical Properties and Radiative Forcing

[54] The model optical and radiative properties are described in the work of K99; however, they now include a new radiative scheme that incorporates relative humidity (RH) dependence [*Schmidt et al.*, 2006]. The optical thickness is dependent on RH via changes in particle size, including deliquescence effects [*Tang and Munkelwitz*, 1991, 1994; *Tang*, 1996] and changes in particle density and refractive index. We assume dry effective radii of $0.2\text{ }\mu\text{m}$ for sulfate; radii for sea salt are derived from the respective model bin sizes, 0.44 and $1.7\text{ }\mu\text{m}$ for small and large sea salt. In the radiative forcing calculations the relative humidity dependence varies with wavelength. Look-up tables of Mie scattering coefficients are used for RH ranging from 0 to 0.999 for each aerosol type. Some sample values of the model mass extinction efficiency (at 550 nm) for sulfate ($0.2\text{ }\mu\text{m}$ dry radius) are 4.67 , 6.9 , 10.2 , 13 , 26 , and $77\text{ m}^2\text{g}^{-1}$ for RH of 25, 50, 75, 85, 95, and 99% RH. For our smaller sea-salt bin ($0.44\text{ }\mu\text{m}$ dry radius), the respective extinction efficiencies are 2.4 , 5.5 , 7.7 , 9.6 , 17 and $47\text{ m}^2\text{g}^{-1}$. Scattering of solar radiation is calculated using the doubling-adding method [*Lacis and Hansen*, 1974].

[55] The annual average optical thicknesses at 550 nm for sulfate and sea salt are shown in Figure 17. We also show the sulfate optical thickness from a natural or preindustrial (PI) simulation, in which we turned off anthropogenic emissions and assumed the biomass burning is $1/2$ the present day burning. As we see in the figure, $1/2$ of the present day (PD) sulfate τ in this simulation is from natural sources, approximately proportional to the fraction of natural burden. The volcanic emissions are apparent in the PI sulfate near Central America, the Mediterranean, Japan and Indonesia. Biomass burning in central Africa is also evident in the optical thicknesses for both the PI and PD simulations. K99 had lower τ (0.027) even though the sulfate burden was greater than it is here; the higher mean τ in this simulation (0.034) is due to the strong increase at very high RH. *Chin et al.* [2002] had a higher sulfate τ of 0.04 (with a higher sulfate burden of 0.57 Tg S compared with our sulfate burden of 0.47 Tg S).

[56] Sea-salt τ is dominated by the smaller size, as seen in the comparison of the bottom pairs of panels in Figure 17. The impact of the RH dependence is evident when we compare the clear-sky and all-sky optical thicknesses, with mean values of 0.044 and 0.12 , respectively. (Clear-sky optical thickness is determined by multiplying the optical thickness by the cloud-free fraction during each radiation time step, then normalizing the monthly mean τ by the mean cloud-free fraction.) Since the RH is less when clouds are not present, the clear-sky optical thickness is much less

(by a factor of about 2.5) than the all-sky τ . Again we compare with *Chin et al.* [2002] who have a higher burden than we do ($8\text{--}14\text{ Tg}$ compared with our 5 Tg) but a lower τ of 0.027 . Since τ validation is done primarily using satellite and Sun photometer measurements under clear-sky conditions, it is difficult to determine whether our all-sky results are excessive. However, we may compare our clear-sky optical thickness with satellite-retrieved values. In the southern oceans sea salt and sulfate should dominate the aerosol optical thickness. From $30\text{--}60^\circ\text{S}$, optical thicknesses based on MODIS is 0.11 and the GISS model has an average of 0.15 [*Yu et al.*, 2006]. From $0\text{--}30^\circ\text{S}$ over the Pacific, the MODIS estimate is $\tau = 0.09$ and the model is 0.04 . However, in this region biomass burning may play an important role.

[57] The annual mean shortwave, top-of-the-atmosphere (TOA) sea salt and sulfate radiative forcings are shown in Figure 18. The sea-salt radiative forcing is substantial; however, since it presumably changes little between preindustrial and present day it does not induce climate change. The anthropogenic direct radiative forcing for sulfate is shown in the top panel, and is found by subtracting the PI from the PD sulfate forcing. (We show the direct sulfate forcing only.) The annual mean anthropogenic sulfate forcing (-0.25 W m^{-2}) is lower than that of K99 (-0.68 W m^{-2}) because of the smaller industrial emissions assumed here. Previous estimates of anthropogenic sulfate radiative forcing were shown by *Adams et al.* [2001, Figure 1] in a figure of anthropogenic forcing versus anthropogenic sulfate burden. The figure has a range of estimated forcings between -0.25 and -1 W m^{-2} and a range of anthropogenic sulfate burdens between 0.3 and 0.56 Tg S . Our result (our anthropogenic sulfate burden is 0.23 Tg S) falls squarely in the middle of the envelope of previous estimates; however, our forcing is among the lowest and our anthropogenic burden is lowest. The addition of heterogeneous oxidation of sulfate on dust [*Bauer and Koch*, 2005] increases the sulfate burden by about 10%, but since more sulfate is coating dust, the anthropogenic sulfate forcing is reduced to -0.18 W m^{-2} .

7. Conclusions

[58] We have presented the results of the current GISS ModelE aerosol simulations. We have worked simultaneously with anthropogenic sulfur species and with natural species in order to increase our insight into the model processes influencing the aerosol distributions.

[59] The new GCM aerosol simulation has several improvements, including increased vertical resolution and the addition of a dissolved species budget (for stratiform clouds). The DSB increases aerosol removal by precipitation and therefore reduces aerosol loads by up to $1/3$. The DSB has a large impact on species over the oceans, especially sea salt since it forms just above the ocean surface and frequently beneath clouds. MSA and sea-salt loads were 23% and 34% less with the DSB. The impact is also particularly great for sulfate since it is generated and rained out by clouds. The simulation with the DSB has about 30% less sulfate, a result similar to our previous study that used a DSB for sulfate [*Koch et al.*, 2003]. For ^{210}Pb the DSB had a lower impact: about 15% reduction of ^{210}Pb .

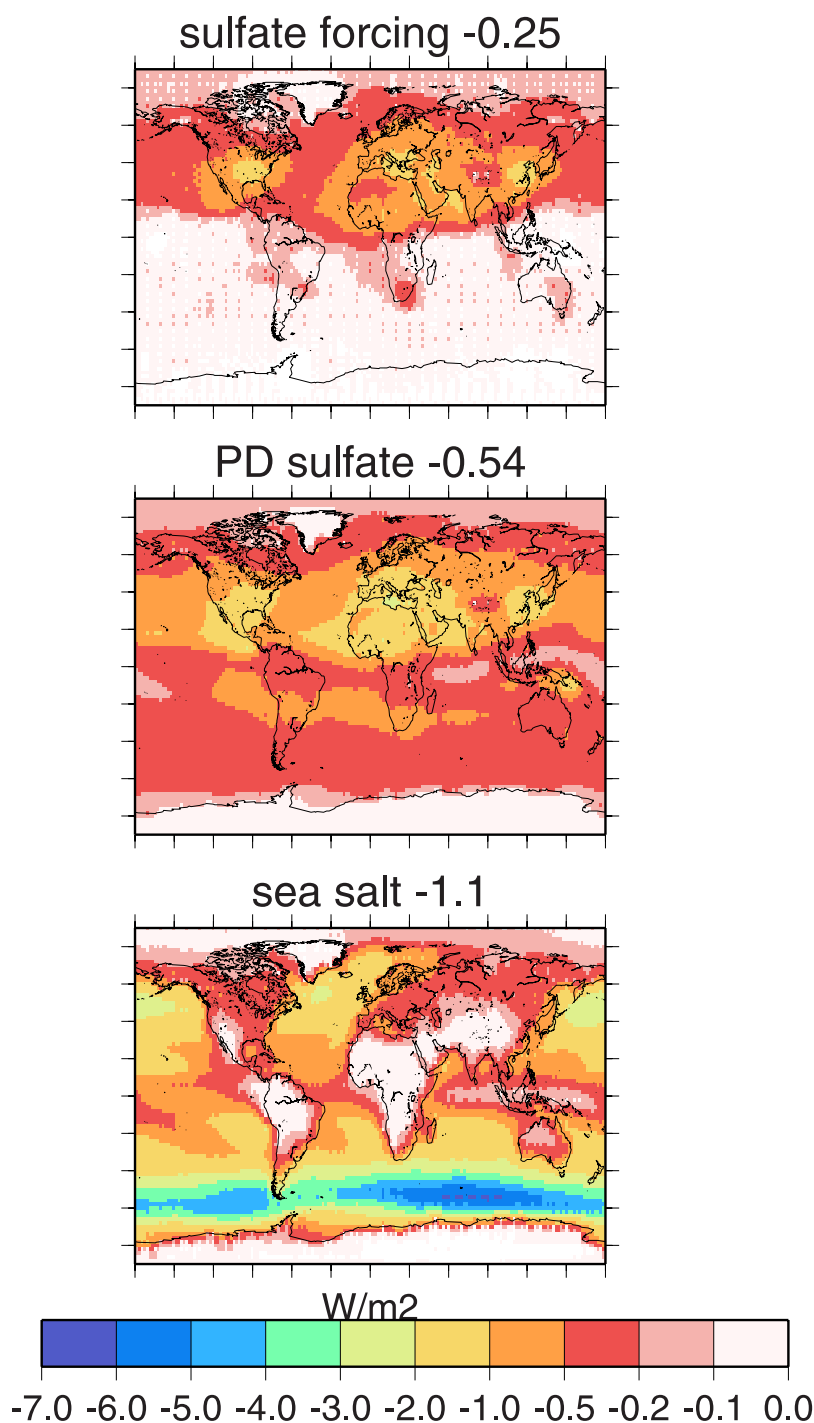


Figure 18. Annual mean shortwave TOA radiative forcing for sea salt (bottom), present-day sulfate (middle), and the anthropogenic sulfate forcing (top).

Since ^{210}Pb forms from the decay of radon and radon has a sufficiently long lifetime (about 5 days on average) to frequently escape the boundary layer and therefore rise above clouds, this reduces the impact of the DSB on the global mean ^{210}Pb load. In addition, ^7Be , which descends to the surface typically with convective subsidence was not significantly affected by the DSB (about 2% less with the DSB). Indeed it appears that the radionuclide aerosols are more sensitive to changes in model convective transport and

scavenging than they are to changes in the stratiform scheme (the DSB).

[60] Our ^{210}Pb has a positive bias (factor of 2 overall), although it captures remote concentrations quite well. Older models [Rasch *et al.*, 2000a] tended to have deficient ^{210}Pb concentrations in remote regions. Compared with a few surface sites, the radon bias does not appear to be excessive. Thus our ^{210}Pb bias suggests that either we should be scavenging more efficiently, or that radon emissions are

too great in regions where we have not compared with radon observations. Using the B93 emission (constant emission from land with 1/3 reduction for frozen land) resulted in excessive ^{210}Pb during summer at high latitudes. The previous GISS-derived CTM (B93) did not have this difficulty. However, that version of the GISS model had excessive convective activity over land, and most convective events originated in the lowest layer (due to its coarse vertical resolution). This summertime moist convection efficiently sucked the ^{210}Pb from the lowest layer and scavenged it, so there was no positive summertime ^{210}Pb bias. Our current model version, with double resolution in the boundary layer, frequently has convection originating above the lowest model layer. As a result it does not scavenge surface-level ^{210}Pb as efficiently.

[61] Of the 3 radon emissions we used, we found least tropospheric bias using that of CR02 (with a linear reduction of radon emission from 30°N to 70°N). CR02 did not specify whether radon emission should be suppressed under freezing conditions. We found that high-latitude seasonality was optimal without this suppression, supporting the suggestion of CR02 that radon emission reduction at high latitudes results from other factors such as soil type and moisture. Optimal correlation between model radon and observations and lowest ^{210}Pb bias in the stratosphere were obtained using a reduced version of SW98. A study by Gupta *et al.* [2004] considered 3 radon emissions: the emission of Rasch *et al.* [2000a], CR02 and the Rasch *et al.* [2000a] emission reduced by a factor of 0.72. Comparing with radon observations, they found that the first 2 performed best in the Northern Hemisphere, but the third emission performed best in the Southern Hemisphere. These results are similar to our findings, that the CR02 performed best in the NH, while the mSW98 (with less SH emissions) performed best in the SH and stratosphere.

[62] The current model ^7Be is improved in some respects (compared to K96). In K96 the tropical surface concentrations were too high because the model convection did not entrain (and scavenge) free tropospheric aerosols and thus delivered excessive ^7Be to the surface. In the current model this is corrected so that the latitudinal gradient is now captured. The model of Liu *et al.* [2001] also had appropriately suppressed tropical ^7Be surface concentrations; they attribute their success to precipitating cloud anvils. On the other hand, our current model has low bias (factor of 2) in the upper troposphere and lower stratosphere while agreeing well with surface concentrations. This suggests that our current source is too small, and that either the model delivers too much Beryllium to the surface and/or does not scavenge efficiently enough.

[63] Our simple 2-bin sea-salt simulation appears to give us reasonably good results compared with available observations. It was helpful to work with 2 wind-derived particulate species, MSA (oxidized from DMS) and sea salt, especially since many of the data were co-located. In the windy sub-Antarctic region both species were overpredicted by the model. In the case of MSA the bias occurs in summertime when DMS ocean concentrations are largest. The sea-salt bias is greatest in winter when the winds are maximum. These wind-derived species are excessive in the southern oceans and not in windy regions of the NH. This may be because of the large SH source region combined

with the model's relatively long aerosol lifetimes [Textor *et al.*, 2005]. Model sea-salt concentrations in other (low latitude) regions have a tendency to be less than observed.

[64] Our sulfur simulation is very different from that of K99, our previous model. We use new emissions and although the total emissions are similar, we now have less anthropogenic and greater natural emissions. The anthropogenic SO_2 emissions used here are for the year 2000 (53 Tg S yr^{-1}) and the K99 emissions were for the year 1985 (65 Tg S yr^{-1}). The natural DMS and volcanic sulfur emissions are increased so that a greater fraction (about 1/2) of the total sulfate burden is natural compared with K99 (about 1/4). The DSB also contributes to this because the natural emissions more readily escape to the free troposphere and are therefore less subject to stratiform precipitation scavenging. The change in emissions and the DSB causes the burden to be less: 0.47 Tg S compared with 0.73 in K99. However, the new relative humidity-dependent radiative scheme generates a substantial hydrated optical thickness so that our new average sulfate optical thickness is 0.034 while that in K99 was 0.027 . The anthropogenic radiative forcing is greatly reduced (-0.25 W m^{-2} , compared with -0.68 W m^{-2} in K99), due to the decreased anthropogenic sulfate fraction.

[65] The DSB has caused our sulfate model concentrations to be less than observed in many regions. This does not disturb us since there still appears to be more than enough SO_2 available to make more sulfate. A mechanism not included in the model here, but presented in a companion paper [Bauer and Koch, 2005] shows that including heterogeneous oxidation production of sulfate on dust increases the sulfate load by about 10% globally, with large impacts where dust is available. Several field studies suggest that dust, sea salt and black carbon are often coated with sulfate [e.g., Zhuang *et al.*, 1999, 2000; Savoie and Prospero, 1982; Savoie *et al.*, 1989; Clarke *et al.*, 2004]. In addition, other oxidants may play important roles in sulfate production, such as ozone [Barth *et al.*, 2000; Rotstajn and Lohmann, 2002] and catalytic oxidation by metals (e.g., MnII and FeIII) [Berglen *et al.*, 2004], especially in regions and seasons with limited photo-oxidants availability. Such mechanisms and oxidants will be pursued in future studies.

[66] **Acknowledgments.** This work is supported by the NASA Climate Modeling Program and by the NSF grant ATM-03-17562. We thank Joseph Prospero and Dennis Savoie for providing their oceanic aerosol data set. We thank Carolyn Jordan and Jack Dibb for sharing their radionuclide aircraft data. We thank Franz Conen and Steve Schery for advice on radon emissions and Wlodek Zahorowski for his radon data set. We thank Steve Schery and Shoichi Taguchi for helpful comments on the manuscript. We gratefully acknowledge the data provision from the following networks: EANET (www.adorc.gr.jp), IMPROVE (vista.cira.colostate.edu/IMPROVE), EML/HASP (www.eml.doe.gov/databases/hasp), EML/SASP (www.eml.doe.gov/databases/sasp), EML radon (www.eml.doe.gov/databases/radon), EMEP (www.emep.int), and GTE aircraft data (www.gte.larc.nasa.gov).

References

- Adams, P. J., J. H. Seinfeld, D. Koch, L. Mickley, and D. Jacob (2001), General circulation model assessment of direct radiative forcing by the sulfate-nitrate-ammonium-water inorganic aerosol system, *J. Geophys. Res.*, **106**, 1097–1111.
- Allen, D. J., R. B. Rood, A. M. Thompson, and R. D. Hudson (1996), Three-dimensional Rn-222 calculations using meteorological data and a convective mixing algorithm, *J. Geophys. Res.*, **101**, 6871–6881.

- Andres, R. J., and A. D. Kasgnoc (1998), A time-averaged inventory of subaerial volcanic sulfur emissions, *J. Geophys. Res.*, **103**, 25,251–25,262.
- Balkanski, Y. J., D. J. Jacob, G. M. Gardner, W. C. Graustein, and K. K. Turekian (1993), Transport and residence times of tropospheric aerosols inferred from a global three-dimensional simulation of ^{210}Pb , *J. Geophys. Res.*, **98**, 20,573–20,586.
- Barrie, L. A., et al. (2001), A comparison of large scale atmospheric sulfate aerosol models (COSAM): Overview and highlights, *Tellus, Ser. B*, **53**, 615–645.
- Barth, M., P. J. Rasch, J. T. Kiehl, C. M. Benkovitz, and S. E. Schwartz (2000), Sulfur chemistry in the National Center for Atmospheric Research Community Climate Model: Description, evaluation, features and sensitivity to aqueous chemistry, *J. Geophys. Res.*, **105**, 1387–1415.
- Bauer, S. E., and D. Koch (2005), Impact of heterogeneous sulfate formation at mineral dust surfaces on aerosol loads and radiative forcing in the Goddard Institute for Space Studies general circulation model, *J. Geophys. Res.*, **110**, D17202, doi:10.1029/2005JD005870.
- Bell, N., D. Koch, and D. T. Shindell (2005), Impacts of chemistry-aerosol coupling on tropospheric ozone and sulfate simulations in a general circulation model, *J. Geophys. Res.*, **110**, D14305, doi:10.1029/2004JD005538.
- Berglen, T. F., T. K. Berntsen, I. S. A. Isaksen, and J. K. Sundet (2004), A global model of the coupled sulfur/oxidant chemistry in the troposphere: The sulfur cycle, *J. Geophys. Res.*, **109**, D19310, doi:10.1029/2003JD003948.
- Brost, R. A., J. Feichter, and M. Heimann (1991), Three-dimensional simulation of ^7Be in a global climate model, *J. Geophys. Res.*, **96**, 22,423–22,445.
- Chin, M., and D. J. Jacob (1996), Anthropogenic and natural contributions to tropospheric sulfate: A global model analysis, *J. Geophys. Res.*, **101**, 18,691–18,700.
- Chin, M., D. J. Jacob, G. M. Gardner, M. S. Foreman-Fowler, P. A. Spiro, and D. L. Savoie (1996), A global three-dimensional model of tropospheric sulfate, *J. Geophys. Res.*, **101**, 18,667–18,690.
- Chin, M., R. B. Rood, S.-J. Lin, J.-F. Muller, and A. M. Thompson (2000a), Atmospheric sulfur cycle simulated in the global model GOCART: Model description and global properties, *J. Geophys. Res.*, **105**, 24,671–24,687.
- Chin, M., D. L. Savoie, B. J. Huebert, A. R. Bandy, D. C. Thornton, T. S. Bates, P. K. Quinn, E. S. Saltzman, and W. J. DeBruyn (2000b), Atmospheric sulfur cycle simulated in the global model GOCART: Comparison with field observations and regional budgets, *J. Geophys. Res.*, **105**, 24,689–24,712.
- Chin, M., P. Ginoux, S. Kinne, O. Torres, B. N. Holben, B. N. Duncan, R. V. Martin, J. A. Logan, A. Higurashi, and T. Nakajima (2002), Tropospheric aerosol optical thickness from the GOCART model and comparisons with satellite and Sun photometer measurements, *J. Atmos. Sci.*, **59**, 461–483.
- Clarke, A. D., et al. (2004), Size distributions and mixtures of dust and black carbon aerosol in Asian outflow: Physiochemistry and optical properties, *J. Geophys. Res.*, **109**, D15S09, doi:10.1029/2003JD004378.
- Conen, F., and L. B. Robertson (2002), Latitudinal distribution of radon-222 flux from continents, *Tellus, Ser. B*, **54**, 127–133.
- Feichter, J., R. A. Brost, and M. Heimann (1991), Three-dimensional modeling of the concentration and deposition of ^{210}Pb aerosols, *J. Geophys. Res.*, **96**, 22,447–22,460.
- Feichter, J., E. Kjellström, H. Rodhe, F. Dentener, J. Lelieveld, and G.-J. Roelofs (1996), Simulation of the tropospheric sulfur cycle in a global climate model, *Atmos. Environ.*, **30**, 1693–1707.
- Gerber, H. E. (1985), Relative-humidity parameterization of the Navy aerosol model (NAM), *NRL Rep. 8956*, Natl. Res. Lab., Washington, D. C.
- Gong, S. L., L. A. Barrie, and J.-P. Blanchet (1997), Modeling sea-salt aerosols in the atmosphere: 1. Model development, *J. Geophys. Res.*, **102**, 3805–3818.
- Graf, H.-F., J. Feichter, and B. Langmann (1997), Volcanic sulfur emissions: Estimates of source strength and its contribution to the global sulfate distribution, *J. Geophys. Res.*, **102**, 10,727–10,738.
- Gupta, M., A. R. Doublas, S. R. Kawa, and S. Pawson (2004), Use of radon for evaluation of atmospheric transport models: Sensitivity to emissions, *Tellus, Ser. B*, **56**, 404–412.
- Halmer, M. M., H.-U. Schmincke, and H.-F. Graf (2002), The annual volcanic gas input into the atmosphere, in particular into the stratosphere: A global data set for the past 100 years, *J. Volcanol. Geoth. Res.*, **115**, 511–528.
- Jacob, D. J., and M. J. Prather (1990), Radon-222 as a test of boundary layer convection in a general circulation model, *Tellus, Ser. B*, **42**, 118–134.
- Jacob, D. J., et al. (1997), Evaluation and intercomparison of global atmospheric transport models using ^{222}Rn and other short-lived tracers, *J. Geophys. Res.*, **102**, 5953–5970.
- Jordan, C. E., J. E. Dibb, and R. C. Finkel (2003), $^{10}\text{Be}/^7\text{Be}$ tracer of atmospheric transport and stratosphere-troposphere exchange, *J. Geophys. Res.*, **108**(D8), 4234, doi:10.1029/2002JD002395.
- Kettle, A. J., et al. (1999), A global database of sea surface dimethylsulfide (DMS) measurements and a procedure to predict sea surface DMS as a function of latitude, longitude and month, *Global Biogeochem. Cycles*, **13**, 394–444.
- Koch, D. (2001), Transport and direct radiative forcing of carbonaceous and sulfate aerosols in the GISS GCM, *J. Geophys. Res.*, **106**, 20,311–20,332.
- Koch, D., and J. Hansen (2005), Distant origins of Arctic black carbon: A Goddard Institute for Space Studies ModelE experiment, *J. Geophys. Res.*, **110**, D04204, doi:10.1029/2004JD005296.
- Koch, D., and D. Rind (1998), Beryllium 10/beryllium 7 as a tracer of stratospheric transport, *J. Geophys. Res.*, **103**, 3907–3917.
- Koch, D., D. J. Jacob, and W. C. Graustein (1996), Vertical transport of tropospheric aerosols as indicated by ^7Be and ^{210}Pb in a chemical tracer model, *J. Geophys. Res.*, **101**, 18,651–18,666.
- Koch, D., D. Jacob, I. Tegen, D. Rind, and M. Chin (1999), Tropospheric sulfur simulation and sulfate direct radiative forcing in the Goddard Institute for Space Studies general circulation model, *J. Geophys. Res.*, **104**, 23,799–23,822.
- Koch, D., J. Park, and A. Del Genio (2003), Clouds and sulfate are anticorrelated: A new diagnostic for global sulfur models, *J. Geophys. Res.*, **108**(D24), 4781, doi:10.1029/2003JD003621.
- Lacis, A. A., and J. E. Hansen (1974), A parameterization for the absorption of solar radiation in the Earth's atmosphere, *J. Atmos. Sci.*, **31**, 118–133.
- Lal, D., and B. Peters (1967), Cosmic ray produced radioactivity on the Earth, *Hand. Phys.*, **46**, 551–612.
- Land, C., and J. Feichter (2003), Stratosphere-troposphere exchange in a changing climate simulated with the general circulation model MAECHAM4, *J. Geophys. Res.*, **108**(D12), 8523, doi:10.1029/2002JD002543.
- Lee, H. N., and J. Feichter (1995), An intercomparison of wet precipitation scavenging schemes and the emission rates of ^{222}Rn for the simulation of global transport and deposition of ^{210}Pb , *J. Geophys. Res.*, **100**, 23,253–23,270.
- Liu, H., D. J. Jacob, I. Bey, and R. M. Yantosca (2001), Constraints from ^{210}Pb and ^7Be on wet deposition and transport in a global three-dimensional chemical tracer model driven by assimilated meteorological winds, *J. Geophys. Res.*, **106**, 12,109–12,128.
- Lohmann, U., et al. (2001), Comparison of the vertical distributions of sulfur species from models participated in the COSAM exercise with observations, *Tellus, Ser. B*, **53**, 646–672.
- Mahowald, N. M., P. J. Rasch, B. E. Eaton, S. Whittlestone, and R. G. Prinn (1997), Transport of ^{222}Rn to the remote troposphere using the Model of Atmospheric Transport and Chemistry and assimilated winds from ECMWF and the National Center for Environmental Prediction/NCAR, *J. Geophys. Res.*, **102**, 28,139–28,151.
- Masarik, J., and J. Beer (1999), Simulation of particle fluxes and cosmogenic nuclide production in the Earth's atmosphere, *J. Geophys. Res.*, **104**, 12,099–12,111.
- Monahan, E. C., D. E. Spiel, and K. L. Davidson (1986), A model of marine aerosol generation via whitecaps and wave disruption, in *Oceanic Whitecaps*, edited by E. C. Monahan and G. Mac Niocaill, pp. 167–174, Springer, New York.
- Nightingale, P. D., G. Malin, C. S. Law, A. J. Watson, P. S. Liss, M. I. Liddicoat, J. Boutin, and R. C. Upstill-Goddard (2000), In situ evaluation of air-sea exchange parameterizations using novel conservative and volatile tracers, *Global Biogeochem. Cycles*, **14**, 373–387.
- Rasch, P. J., et al. (2000a), A comparison of scavenging and deposition processes in global models: Results from the WCCRP Cambridge Workshop of 1995, *Tellus, Ser. B*, **52**, 1025–1056, doi:10.1034/j.1600-0889.2000.00980.
- Rasch, P. J., M. C. Barth, J. T. Kiehl, S. E. Schwartz, and C. M. Benkovitz (2000b), A description of the global sulfur cycle and its controlling processes in the National Center for Atmospheric Research Community Climate Model, Version 3, *J. Geophys. Res.*, **105**, 1367–1385.
- Rehfeld, S., and M. Heimann (1995), Three-dimensional atmospheric transport simulation of the radioactive tracers ^{210}Pb , ^7Be , ^{10}Be , and ^{90}Sr , *J. Geophys. Res.*, **100**, 26,141–26,161.
- Roelofs, G.-J., et al. (2001), Analysis of regional budgets of sulfur species modelled for the COSAM exercise, *Tellus, Ser. B*, **53**, 673–694.
- Rotstajn, L. D., and U. Lohmann (2002), Simulation of the tropospheric sulfur cycle in a global model with a physically based cloud scheme, *J. Geophys. Res.*, **107**(D21), 4592, doi:10.1029/2002JD002128.

- Savoie, D. L., and J. M. Prospero (1982), Particle size distribution of sulfate and nitrate in the marine atmosphere, *Geophys. Res. Lett.*, **9**, 1207–1210.
- Savoie, D. L., J. M. Prospero, and E. S. Saltzman (1989), Non-sea-salt sulfate and nitrate in trade wind aerosols at Barbados: Evidence for long-range transport, *J. Geophys. Res.*, **94**, 5069–5080.
- Schery, S. D., and M. A. Wasiolek (1998), Modeling ^{222}Rn flux from the earth's surface, in *The Human Environment*, edited by A. Katase and M. Shimo, pp. 207–217, World Scientific, Tokyo.
- Schmidt, G. A., et al. (2006), Present day atmospheric simulations using GISS ModelE: Comparison to in-situ, satellite and reanalysis data, *J. Clim.*, **19**, 153–192.
- Takemura, T., H. Okamoto, Y. Maruyama, A. Numaguti, A. Higurashi, and T. Nakjima (2000), Global three-dimensional simulation of aerosol optical thickness distribution of various origins, *J. Geophys. Res.*, **105**, 17,853–17,873.
- Tang, I. N. (1996), Chemical and size effects of hygroscopic aerosols on light scattering coefficients, *J. Geophys. Res.*, **101**, 19,245–19,250.
- Tang, I. N., and H. R. Munkelwitz (1991), Simultaneous determination of refractive index and density of an evaporating aqueous solution droplet, *Aerosol Sci. Technol.*, **15**, 201–207.
- Tang, I. N., and H. R. Munkelwitz (1994), Water activities, densities, and refractive indices of aqueous sulfates and sodium nitrate droplets of atmospheric importance, *J. Geophys. Res.*, **99**, 18,801–18,808.
- Textor, C., et al. (2005), Analysis and quantification of the diversities of aerosol life cycles within AeroCom, *Atmos. Chem. Phys. Disc.*, **5**, 8331–8420.
- Yu, H., et al. (2006), A review of measurement-based assessment of aerosol direct radiative effect and forcing, *Atmos. Chem. Phys.*, **6**, 613–666.
- Zahorowski, W., S. Chambers, T. Wang, C.-H. Kang, I. Uno, S. Poon, S.-N. Oh, S. Werczynynski, J. Kim, and A. Henderson-Sellers (2005), Radon-222 in boundary layer and free tropospheric continental outflow events at three ACE-Asia sites, *Tellus, Ser. B*, **57**, 124–140.
- Zaucker, F., P. H. Daum, U. Wetterauer, C. Berkowitz, B. Dromer, and W. S. Broecker (1996), Atmospheric ^{222}Rn measurements during the 1993 NARE Intensive, *J. Geophys. Res.*, **101**, 29,149–29,164.
- Zhuang, D., G.-Y. Shi, Y. Iwasaka, and M. Hu (2000), Mixture of sulfate and nitrate in coastal atmospheric aerosols: Individual particle studies in Qingdao (36°04' 102°21'E), China, *Atmos. Environ.*, **34**, 2669–2679.
- Zhuang, H. C., C. K. Chan, M. Fang, and A. S. Wexler (1999), Formation of nitrate and non-sea-salt sulfate on coarse particles, *Atmos. Environ.*, **33**, 4223–4233.

D. Koch, G. A. Schmidt, and C. V. Field, NASA Goddard Institute for Space Studies, Columbia University, 2880 Broadway, New York, NY 10025, USA. (dkoch@giss.nasa.gov)